



5-2013

A search for volatile ices on the surfaces of cold classical Kuiper Belt Objects

Daine Michael Wright
dwright14@utk.edu

Follow this and additional works at: https://trace.tennessee.edu/utk_gradthes



Part of the [Other Astrophysics and Astronomy Commons](#), and the [The Sun and the Solar System Commons](#)

Recommended Citation

Wright, Daine Michael, "A search for volatile ices on the surfaces of cold classical Kuiper Belt Objects. " Master's Thesis, University of Tennessee, 2013.
https://trace.tennessee.edu/utk_gradthes/1699

This Thesis is brought to you for free and open access by the Graduate School at TRACE: Tennessee Research and Creative Exchange. It has been accepted for inclusion in Masters Theses by an authorized administrator of TRACE: Tennessee Research and Creative Exchange. For more information, please contact trace@utk.edu.

To the Graduate Council:

I am submitting herewith a thesis written by Daine Michael Wright entitled "A search for volatile ices on the surfaces of cold classical Kuiper Belt Objects." I have examined the final electronic copy of this thesis for form and content and recommend that it be accepted in partial fulfillment of the requirements for the degree of Master of Science, with a major in Geology.

Joshua Emery, Major Professor

We have read this thesis and recommend its acceptance:

Harry McSween, Jeffrey Moersch

Accepted for the Council:

Carolyn R. Hodges

Vice Provost and Dean of the Graduate School

(Original signatures are on file with official student records.)

**A search for volatile ices on the
surfaces of cold classical Kuiper Belt
Objects**

A Thesis Presented for
The Master of Science
Degree

The University of Tennessee, Knoxville

Daine Michael Wright

May 2013

© by Daine Michael Wright, 2013
All Rights Reserved.

This thesis is dedicated to my father, David Wright, who fueled my interest in science from my first observation of the viscosity of ketchup.

Acknowledgments

My mentors and teachers at the University of Tennessee have been invaluable in my education. Thomas Handler took me under his wing early in my career as a student and taught me that knowledge requires application. Jeff Moersch and Hap McSween provided insightful guidance and suggestions during my research and the writing of this thesis. Josh Emery lead me out into the far reaches of the Solar System and forced me think for myself. My parents, David and Connie, gave me a strong foundation of curiosity from which I could build my scientific knowledge. Finally and most importantly, my wonderful wife, Courtney, has given me the motivation, confidence, and resources to buckle down and complete this work.

Abstract

The surprisingly complex dynamical distribution of small bodies among and beyond the orbits of the planets has changed our understanding of Solar System evolution and planetary migration. Compositional information about the small bodies in the Solar System provides constraints for models of Solar System formation. According to most models, the Kuiper Belt population known as the cold classicals formed at distances far enough from the Sun for these objects to be composed of an appreciable fraction of volatile ices of diverse composition (H_2O , CO_2 , CH_4 , light hydrocarbons, e.g. CH_3OH) and their orbits have remained stable. Cold classical objects should still be volatile rich. Broadband data from the *Spitzer Space Telescope* Infrared Array Camera (IRAC) can detect and distinguish between absorptions of relevant ices in the 3-5 μm [micron] infrared region. Of the 46 cold classical Kuiper Belt Objects in this study, 78% of their surfaces exhibit absorptions from ices or organics in IRAC channel 1 (3.6 μm [micron]). The combination of data from IRAC channels 1 and 2 (4.5 μm [micron]) provides gross surface composition for the six objects with secure observations in both channels. These six objects are observed to have ices or organics on their surfaces; this is the first detection of ices on four of these objects. The surface of 20000 Varuna contains organic material. The surface of 50000 Quaoar is confirmed to be rich in water ice. The surface composition of 19521 Chaos is mixed ice and organics. Mixed ices, with a high fraction of water ice, and other components are on the surface of 119951 2002 KX14. The surface of 66652 Borasisi is methane rich. Methanol or light hydrocarbons are on the surface of 138537 2000 OK67. Cold classical objects are found to be volatile rich and of diverse surface composition. The presence of ices and organics indicate these objects formed far from the Sun.

Contents

Introduction	1
1 Background	2
1.1 History of the Kuiper Belt	2
1.2 The Cold Classical Objects	3
2 Observations	8
3 Results	14
3.1 <i>Spitzer</i> IRAC results	14
3.2 Cold classical classification	15
3.3 Vis-NIR data	16
4 Analysis	18
4.1 Absorption at IRAC wavelengths	18
4.2 Surface composition analysis	21
4.2.1 19521 Chaos	27
4.2.2 20000 Varuna	28
4.2.3 50000 Quaoar	28
4.2.4 66652 Borasisi	28
4.2.5 119951 2002 KX14	29
4.2.6 138537 2000 OK67	29
4.3 Correlations with object characteristics	31
5 Discussion	34

Conclusions	39
References	41
A IRAC observational data	52
B Published photometric data	58
C Photometric plots	62
D Database of KBO literature	74
Vita	75

List of Tables

2.1	Orbital circumstances of <i>SST</i> /IRAC observations	9
4.1	Average photometric colors	20
4.2	Objects with negative K-ch1 color	21
4.3	IRAC color indices for cold classical objects	25
4.4	Observed ices	29
5.1	Spectral class in order of K-ch1 index	36
A.1	IRAC fluxes and converted albedos	52
B.1	Published photometric data	58
B.2	Colors published in Trujillo et al. (2011)	60
B.3	<i>HST</i> photometry	61

List of Figures

1.1	Cartoon of nomenclature scheme	4
1.2	Dynamic classification of selected KBOs	5
1.3	Depth of 2 μm band as a proxy for water ice on KBOs	6
1.4	Albedo spectra of selected ices observed on KBOs	7
2.1	Background subtraction from repeated IRAC observations	12
3.1	Spectral plot for 138537 2002 OK67	17
4.1	Spectral plot of 2002 VT130	19
4.2	K-ch1 color indices for cold classical KBOs	22
4.3	Absorption spectra of materials of interest	24
4.4	K-ch1, IRAC color index color-color plot	27
4.5	K-ch1 (average) vs. V-K color indices	30
4.6	Plots of K-ch1 color as a function of orbital parameter	32
4.7	Physical characteristics vs. K-ch1 color	33
C.1	Cold classical KBOs with published K-band data	62
C.2	Cold classical objects with published photometry but no K-band data	63
C.3	Cold classical objects with published photometry but no K-band data, continued	64
C.4	Cold classical objects with some photometry available, but only upper limit IRAC observations	65
C.5	Objects with no published photometry and only upper limit IRAC observations	66
C.6	Cold classical object, 135182 2001 QT322	67
C.7	Photometric plots of objects in MMR with Neptune	67

C.8	Additional objects fitting classification scheme set forth in Petit et al. (2011)	68
C.9	Objects observed with custom filters described in Trujillo et al. (2011)	69
C.10	<i>HST</i> data from Benecchi et al. (2011)	70
C.11	<i>HST</i> data from Benecchi et al. (2009, 2011)	71
C.12	<i>HST</i> data from Fraser and Brown (2012)	72
C.13	<i>HST</i> data from Fraser and Brown (2012), continued	73

Introduction

Just as the history of a rock can be understood by studying radioactive and rare earth elements, which are a negligible part of the rock, the history of the Solar System can be better understood by studying the small planetary bodies. Although the eight large planets dominate the mass of the Solar System, telling a unique story of the Solar System's evolution based on their dynamics or composition is impossible. Small bodies provide significant insight into the formation of the early Solar System, even though their mass is much less (negligible) compared to that of the planets. Because of their large numbers, small bodies are useful test particles for a diverse set of dynamical situations, from early in Solar System history to the current observed state (Tsiganis et al., 2005; Levison et al., 2008; Lykawka and Mukai, 2007). The addition of compositional information adds constraints to complement, guide, and interpret these dynamic models.

It has become evident in recent years that the Kuiper Belt is a fundamental architectural element of the outer Solar System. KBOs are widely considered among the most primitive small bodies in the Solar System. Their compositions thereby provide windows into conditions in the early Solar System, especially at large distance from the Sun. Even with space weathering due to solar radiation, cosmic rays, and interplanetary dust, KBOs represent the most pristine Solar System material observable from Earth (Barucci et al., 2008). Ices are a key component of KBO surfaces. Because these ices have different volatilities, the mixtures of ices on KBO surfaces offer a means to study the origin and evolution of these bodies. Relevant ices exhibit spectral features in the infrared part of the spectrum, which is therefore ideal for investigating the compositions of KBOs.

1. Background

1.1 History of the Kuiper Belt

Pluto was discovered in 1930 by Clyde Tombaugh using a photographic blink comparator. Shortly thereafter, Leonard (1930) suggested Pluto may be the first of the “ultra-Neptunian bodies” awaiting discovery. Edgeworth (1943) suggested that the density in the primordial outer Solar System would be too low to form planets, but rather many small bodies would form a disk similar to the asteroid belt. Kuiper (1951) speculated that a disk would form early in Solar System history. He believed this disk would be scattered by Pluto which he assumed was Earth-sized, and a disk would not currently exist.

For several decades, before the discovery of any other KBOs, only slow advances in thinking about the region past Neptune occurred. For example: Cameron (1962) noted that nebular gas would condense into what he presumed to be comets past Neptune. Whipple (1964a,b) found that the deviation of Neptunes orbit was well explained by a belt or disk of comets past Neptune. Kowal’s discovery of 2060 Chiron orbiting between Saturn and Uranus (Kowal and Gehrels, 1977), fueled new fervor in speculation about a Kuiper Belt and searches for objects past Neptune. Fernandez (1980) calculated properties and proposed mechanisms of depletion for a belt past Neptune based on observations of short period comets.

The introduction of charge-coupled devices (CCDs) allowed for more efficient and sensitive surveys. After years of searching, the first KBO, 15760 1992 QB1, was discovered by Jewitt and Luu (1993) using a computerized blink comparator. The objects beyond Pluto were assumed to be pristine remnants of Solar System formation in undisturbed, cold, circular, low-inclination orbits. The observed orbits of 1992 QB1 and the next object found, 1993 FW (Luu et al., 1993), agreed with the cold, circular orbit assumptions. However

multiple observations of objects 1993 SC, 1993 RO, 1993 RP, and 1993 SB showed that these objects had Pluto-like orbits with eccentricities of around 0.2 (Tholen et al., 1994) and a 3:2 mean-motion resonance with Neptune, clearly not circular. 1999 TL66 (Luu et al., 1997), 1999 CV118, 1999 CY118, and 1999 CF119 (Trujillo and Marsden, 1999), the first of the distant, unstable scattered disk objects, fit into neither the classical or resonant category. With the discovery of these objects, it became apparent that the region beyond Neptune was more complicated than first thought. Large semi-major axis and perihelion objects are found detached from what was thought to be the classical Kuiper Belt; examples of detached objects are 148209 2000 CR105 (Elliot et al., 2005), Sedna (Brown et al., 2004), Eris (Brown et al., 2005), and 2004 XR190 (Allen et al., 2006).

In the present work, the author uses terms Kuiper Belt and Kuiper Belt Object for historical reasons. Alternate names are used by other authors. Edgeworth-Kuiper Belt and Edgeworth-Kuiper Belt Object (EKO) are sometimes used to credit the work by both Edgeworth and Kuiper. Many authors name all of the small bodies Tran-Neptunian Objects (TNOs) to avoid controversy. However this term would include the more distant Oort cloud and disregards the likely origin of Centaurs.

1.2 The Cold Classical Objects

With the discovery of complex and unexpected dynamical properties, dynamical classification of the objects became more complicated than simply trans-Neptunian. As a result of this complexity, several classification schemes exist (cf. Gladman et al., 2008) and objects may be classified differently by different teams. Nevertheless, the main structural features and dynamical parameters are similar in all schemes (fig. 1.1). The classes are generally accepted as Centaurs, resonant, classical, scattered, and extended (fig. 1.2). Centaurs cross the orbit of at least one giant planet. Resonant objects are in stable mean motion resonances (MMRs) with Neptune. The scattered disk objects are those scattered by the giant planets. Detached objects are sufficiently far from the sun to be decoupled from the giant planets. Classical KBOs fit the traditional ideas of the Kuiper Belt. They are confined to ~ 37 to 48 AU.

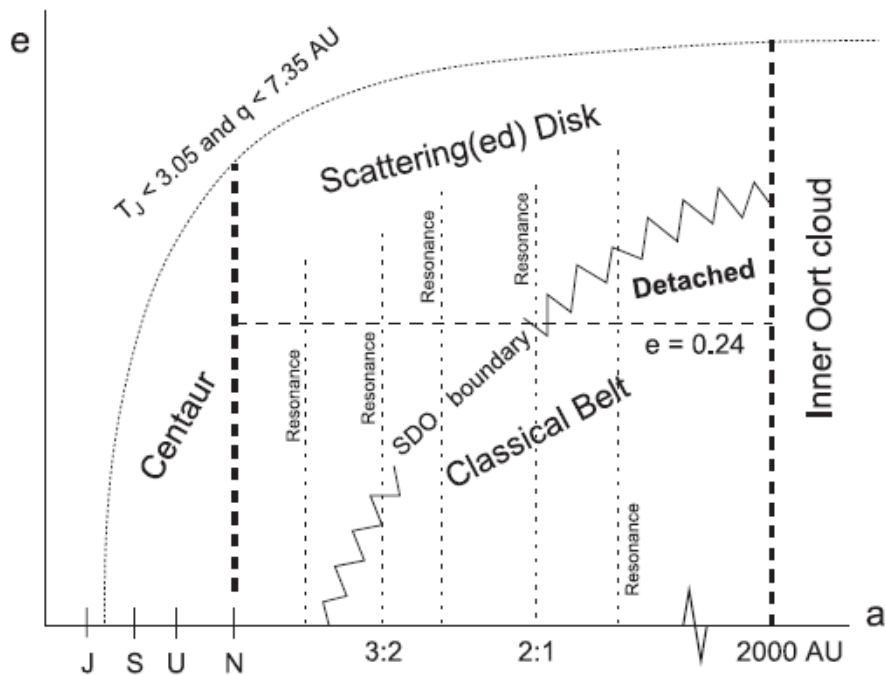


Figure 1.1: Cartoon of nomenclature scheme (not to scale). Boundaries are based on current orbital elements. (Modified from Gladman et al., 2008).

The classical belt is loosely thought of as the belt of planetesimals beyond Neptune leftover from Solar System formation. A bimodal inclination distribution has led to distinct subclasses of “hot” and “cold” classical objects. Dynamically and physically distinct, the cold classical belt objects have low inclination and low eccentricity orbits and comprise the core of the Kuiper Belt. They are not affected by resonances and are thought to have formed roughly where they exist today. The cold classical population is distinct from the other classes in several ways: they have very red spectral slopes in the visible and near-infrared (vis-NIR: $0.4 < \lambda < 1.5 \mu\text{m}$; Tegler and Romanishin, 2000; Trujillo and Brown, 2002), a high fraction of binaries (Noll et al., 2008), and a paucity of larger objects seen in other classes. Even though they may have migrated from 30 to 40 AU (Levison et al., 2008), the cold classical KBOs have remained far enough from the Sun throughout the history of the Solar System that their surfaces have likely not undergone significant thermal evolution compared to other dynamical groups. Because of this, it is reasonable to expect these objects are the most pristine reservoir in the Kuiper Belt, and perhaps the Solar System.

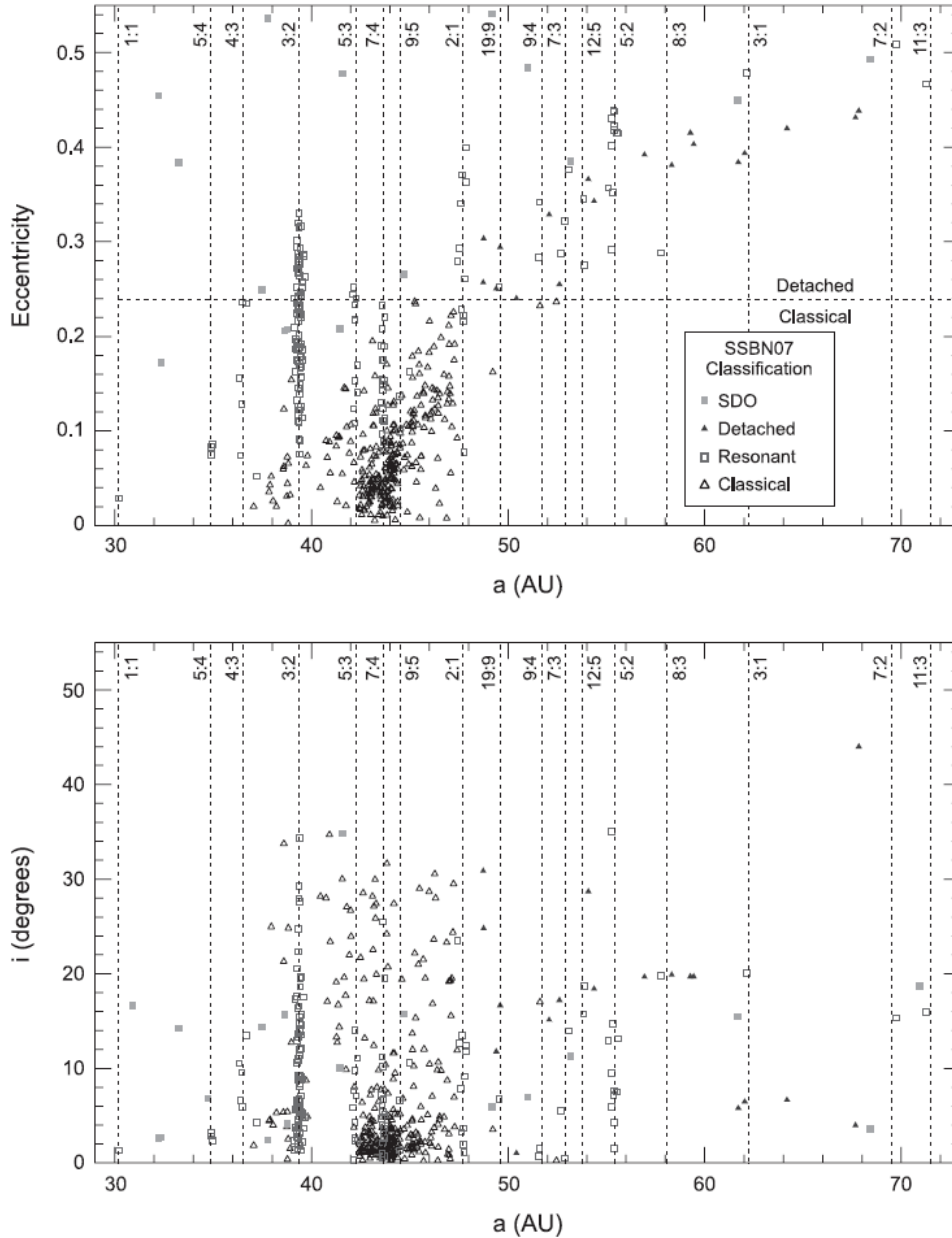


Figure 1.2: Dynamic classification of selected KBOs. Several major MMRs (note 5:3 and 7:4 in the classical belt) are labeled. “Hot” and “cold” classical populations are divided by inclination but not distinguished on this plot. (Modified from Gladman et al., 2008).

Volatiles formed from the solar nebula at these distances. If the cold classical population has been dynamically stable as expected, they should retain the volatiles on their surfaces. The observed dynamical and physical properties of the cold classicals lead to the hypothesis driving the present work: cold classical Kuiper Belt objects are rich in volatiles.

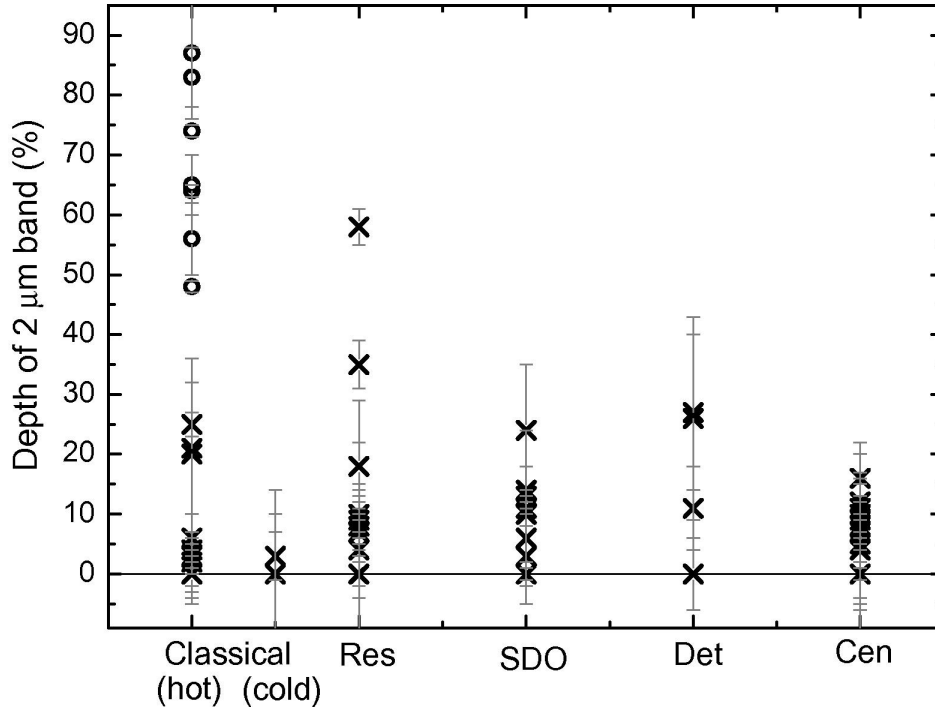


Figure 1.3: Depth of 2 μm band as a proxy for water ice on KBOs from Barucci et al. (2011). Note the cold classical objects exhibit very little absorption, contrary to expectation.

Despite this expectation, Barucci et al. (2011) find no evidence for ice in their sample (3 objects) of cold classical objects (fig. 1.3). They assess the depth of the 2.0 μm water ice band and find the band depth, D , $\leq 3\%$ for all three cold classical objects. They suggest a more sensitive search for volatiles on the surfaces of the cold classical population is needed to assess the presence of ice. 50000 Quaoar is the only object in both our samples for which they report detected ices.

Evidence of volatile ices can be found in IR absorptions identifiable using the 3.6 μm (ch1) and 4.5 μm (ch2) channels of the Infrared Array Camera (IRAC) on board *Spitzer Space Telescope* (*SST*) accompanied by standard JHK filters on terrestrial IR telescopes. Figure 1.4 shows geometric albedo spectra for volatile ices observed or hypothesized ices on KBOs. Note the absorptions of CH_4 and H_2O in IRAC ch1 and CO_2 in ch2. The spectra of these ices are distinguishable from each other with secure IRAC observations. If the cold classical population is found to be poor or depleted in volatiles, particularly compared to other dynamical classes of KBOs, the implication would be that the objects in this population

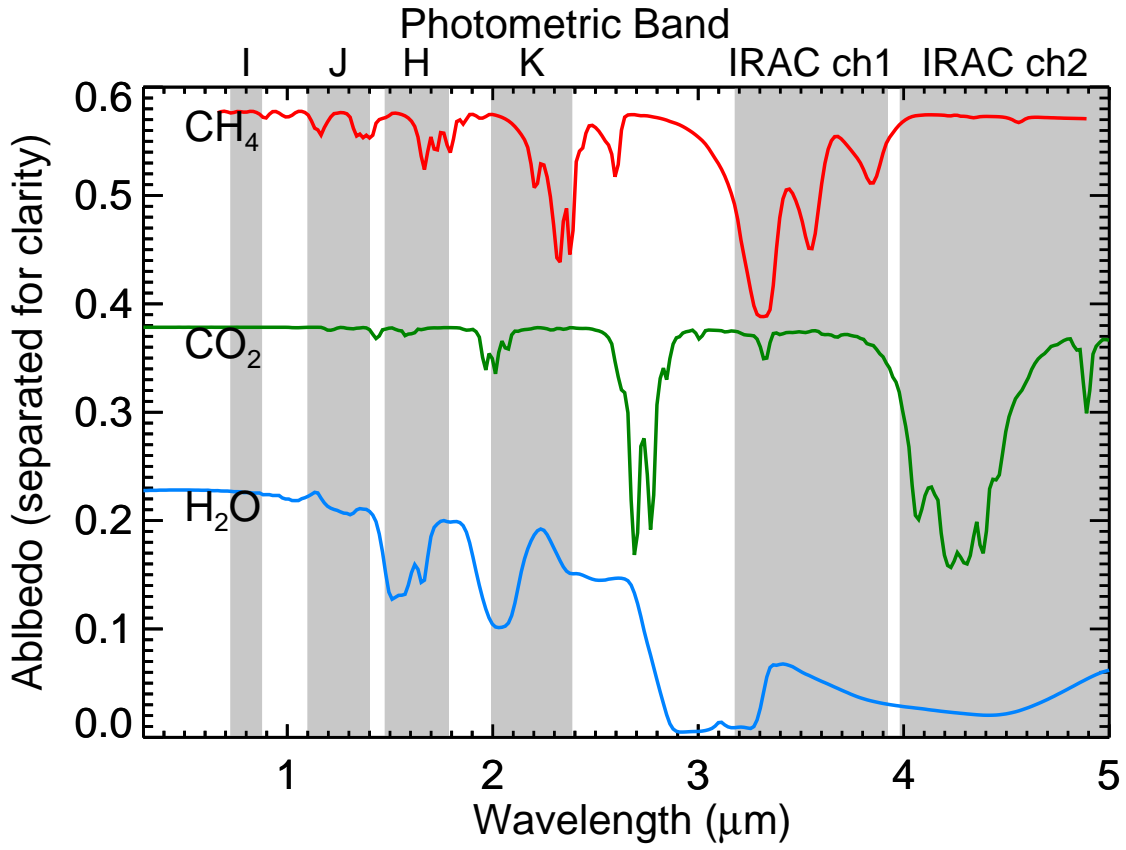


Figure 1.4: Albedo spectra of selected ices observed on KBOs, separated by an arbitrary factor for clarity.

have undergone thermal evolution. Possible sources of thermal evolution are migration to the inner Solar System, complex differentiation, and collisional breakup.

2. Observations

Techniques that are sensitive to the materials that are observed or hypothesized to be on KBOs, such as spectroscopy and photometry, enable the study of surface compositions of KBOs. Reflectance spectroscopy, the study of reflected light as a function of wavelength, is ideal for identifying strong fundamental absorptions caused by transitions and vibrations in the structures of H₂O, CO₂, and CH₄ ices, hydrated silicates, and organics that may be present on the surfaces of KBOs. Vis-NIR reflectance spectra have been measured for many of the brightest KBOs. However, most KBOs are too faint for the measurement of spectra with sufficient sensitivity to identify relevant absorption bands. Broadband photometric measurements are less diagnostic than spectra, but collecting light over a wide range of wavelengths enables observations of much fainter targets. A much larger number of KBOs are bright enough for photometry than are for spectrometry. Assessing similarities with other KBOs provides compositional classifications that lead to better understanding of the surface composition of KBOs.

The wavelengths just longer than the NIR (2.5-10 μm) are dominated by reflected light at temperatures typical in the Kuiper Belt (50 K; Jewitt and Luu, 2004) making this wavelength region useful for spectroscopy and photometry. Even then, most of the cold classical objects are too faint to collect high SNR spectra at longer wavelengths. The broader bandpasses utilized in photometry increase the sensitivity of observations. Many diagnostic absorption features for the materials on the surfaces KBOs occur at $\lambda > 2.5 \mu\text{m}$ and the 3-5 μm region is ideal for detecting and differentiating between relevant ices. *Spitzer* was designed to explore this region.

Spitzer was launched in August 2003 and entered its warm (non-cryogenic) mission in May 2009. *SST* has an aperture of 85 cm and is located in an Earth-trailing, heliocentric

orbit. The Infrared Array Camera (IRAC), a broad-band imager onboard *Spitzer*, has a 5.2 x 5.2 arcmin or 256 x 256 pixel FOV at ~ 1.2 arcsec/pixel. The four broadband channels are centered at 3.6, 4.5, 5.8, and 8.0 μm with widths (FWHM) of 0.68, 0.87, 1.25, and 2.52 μm , respectively (Fazio et al., 2004). During the warm mission, which began in May 2009 when the onboard cryogen was expended, observations only record the flux in ch1 and ch2. Data are available for download from the Spitzer Heritage Archive¹. 46 cold classical KBOs have been observed during the *SST/IRAC* programs. Although some objects were observed in ch3 and ch4, only the ch1 and ch2 data are reported here.

Spitzer collected data from each object on two separate occasions usually several days apart (table 2.1), allowing the object to move ~ 30 arcsec while keeping the object within the same FOV. Each observation consists of nine or more dithered frames. Dithering allows image correction for effects from bad pixels, latent images from previous observations, and stray light from bright objects in or just off the frame. Paired observations provide several benefits: identification of the object by its motion against background stars, straightforward and accurate background subtraction, and increased probability of at least one good measurement in the case of a field star obscuring the object (Emery et al., 2007).

Table 2.1: Orbital circumstances of *SST/IRAC* observations.

Number	Name	Designation	Date	ch1 time ^a	ch2 time ^a	t_{ch1} (min) ^b	t_{ch2} (min) ^b	r (AU) ^c	Δ (AU) ^c	α ($^\circ$) ^c
48639		1995 TL8	3-Mar-11	7:18		103.3		44.1323	43.6618	1.16
			7-Mar-11	19:18			44.1346	43.7342	1.20	
		1996 TK66	4-Sep-09	21:17		46.7		42.9900	42.8142	1.35
			8-Sep-09	23:03			42.9902	42.7470	1.33	
79360	Sila	1997 CS29	7-May-08	23:47	0:08	15.0	53.3	43.5202	43.1181	1.22
			9-May-08	8:37	8:58			43.5202	43.1398	1.23
35671		1998 SN165	29-Jan-10	19:33	20:09	30.0	90.0	37.7497	37.4514	1.47
			3-Feb-10	13:07	13:42					37.7492
19521	Chaos	1998 WH24	19-Oct-07	6:46	7:07	15.0	53.3	41.8486	41.5179	1.34
			23-Oct-07	8:37	8:57					41.8479
		1999 CD158	6-Jun-12	22:20		128.3		47.2322	46.7534	1.07
			12-Jun-12	3:50			47.2307	46.8323	1.12	
		1999 OJ4	6-Dec-09	22:21		53.3		37.9901	37.4749	1.33
	11-Dec-09	3:45				37.9898	37.5381	1.38		
66652	Borasisi	1999 RZ253	26-Dec-07	17:24		106.7	106.7	41.3762	41.3122	1.40
			31-Dec-07	12:10				41.3772	41.3945	1.40
60454		2000 CH105	5-Feb-10	14:10		46.7		43.2203	43.1569	1.34
			9-Feb-10	17:39			43.2194	43.0854	1.33	
		2000 CL104	30-Jan-10	0:11		46.7		43.2576	43.1263	1.33

Continued on next page

¹<http://sha.ipac.caltech.edu/applications/Spitzer/SHA/>

Table 2.1: continued

Number	Name	Designation	Date	ch1 time ^a	ch2 time ^a	t _{ch1} (min) ^b	t _{ch2} (min) ^b	r (AU) ^c	Δ (AU) ^c	α (°) ^c
			3-Feb-10	8:22				43.2584	43.0540	1.31
		2000 CN105	26-Jun-10	14:51	15:27	30.0	106.7	46.5688	46.1645	1.14
			1-Jul-10	4:58	5:34			46.5697	46.2383	1.18
168703		2000 GP183	4-Sep-09	1:17		23.3		36.9892	36.8736	1.58
			7-Sep-09	22:14				36.9895	36.8094	1.56
134860		2000 OJ67	22-Nov-07	8:35		106.7	106.7	42.7297	42.2356	1.20
			25-Nov-07	13:50				42.7299	42.2846	1.23
138537		2000 OK67	13-Jan-10	11:46	12:21	30.0	126.7	40.3171	40.1820	1.43
			17-Jan-10	17:27	18:03			40.3166	40.2534	1.44
		2000 QL251	29-Jan-10	21:50		46.7		39.2828	39.0582	1.44
			3-Feb-10	15:23				39.2846	39.1397	1.46
20000	Varuna	2000 WR106	24-Mar-06	19:20		15.0		43.3078	42.8044	1.15
			29-Mar-06	16:57				43.3085	42.8799	1.20
88268		2001 KK76	23-Sep-09	3:27		46.7		42.1239	41.6214	1.22
			27-Sep-09	22:28				42.1237	41.6933	1.27
		2001 QB298	11-Jan-10	10:01		40.0		39.4903	39.4369	1.47
			15-Jan-10	14:40				39.4910	39.5090	1.47
		2001 QC298	25-Dec-09	0:30		50.0		40.6490	40.1388	1.25
			28-Dec-09	3:29				40.6492	40.1857	1.28
		2001 QD298	7-Dec-09	14:10		30.0		41.4384	40.9255	1.22
			11-Dec-09	3:09				41.4389	40.9789	1.26
		2001 QO297	23-Jan-10	17:42		46.7		43.1844	42.9716	1.31
			27-Jan-10	23:57				43.1840	43.0431	1.33
		2001 QS322	23-Jan-10	12:54	13:30	30.0	103.3	42.3537	42.1175	1.33
			28-Jan-10	1:48	2:24			42.3539	42.1939	1.35
88611	Teharonhiawako		2-Jan-10	4:11		43.3		45.0818	44.9321	1.28
		2001 QT297	6-Jan-10	14:33				45.0819	45.0073	1.29
135182		2001 QT322	23-Jan-10	15:29		30.0	86.7	37.0298	36.7129	1.49
			28-Jan-10	4:23				37.0301	36.7880	1.52
		2001 QX297	11-Jan-10	12:24		46.7		43.3804	43.3151	1.34
			15-Jan-10	15:26				43.3802	43.3851	1.34
275809		2001 QY297	28-Nov-09	18:37		33.3		43.1706	42.7190	1.22
			3-Dec-09	14:33				43.1717	42.7952	1.26
		2001 RZ143	5-Sep-09	18:50		33.3		41.3072	41.2668	1.42
			10-Sep-09	17:50				41.3071	41.1834	1.41
148780	Altjira	2001 UQ18	10-Oct-09	5:44		36.7		45.5202	45.4808	1.29
			14-Oct-09	14:48				45.5209	45.4080	1.29
		2001 XR254	6-Dec-09	8:24		36.7		44.1133	43.9731	1.32
			10-Dec-09	23:36				44.1131	43.8957	1.30
126154		2001 YH140	2-Jan-12	12:00		40.0		36.6747	36.5996	1.59
			6-Jan-12	8:22				36.6753	36.5354	1.58
		2002 GV31	25-Jun-10	5:03	5:23	15.0	60.0	40.2818	39.7718	1.25
			29-Jun-10	14:47	15:07			40.2814	39.8376	1.30
119951		2002 KX14	16-Sep-08	5:56	6:17	15.0	53.3	39.4865	39.2458	1.45
			20-Sep-08	11:40	12:01			39.4860	39.3153	1.47
50000	Quaoar	2002 LM60	15-Sep-05	1:11		26.7		43.3301	43.2765	1.35
			18-Sep-05	7:16				43.3298	43.3304	1.35
		2002 VT130	30-Oct-09	2:10		30.0		42.8637	42.6112	1.33
			3-Nov-09	9:52				42.8641	42.5416	1.31
		2003 GH55	24-Mar-10	4:32		30.0		40.8198	40.7950	1.41
			28-Mar-10	10:07				40.8201	40.7227	1.40
		2003 QA91	9-Dec-09	12:28		36.7		44.8496	44.3340	1.13
			13-Dec-09	2:45				44.8489	44.3873	1.16

Continued on next page

Table 2.1: continued

Number	Name	Designation	Date	ch1 time ^a	ch2 time ^a	t _{ch1} (min) ^b	t _{ch2} (min) ^b	r (AU) ^c	Δ (AU) ^c	α (°) ^c
		2003 QA92	2-Jan-10	3:17		46.7		37.4343	37.2825	1.54
			6-Jan-10	13:39				37.4336	37.3567	1.55
		2003 QR91	28-Nov-09	13:10		50.0		39.2189	38.7047	1.29
			3-Dec-09	15:13				39.2203	38.7827	1.35
		2003 WU188	18-Nov-09	17:03		46.7		43.2478	43.2056	1.36
			22-Nov-09	18:33				43.2482	43.1376	1.35
120347	Salacia	2004 SB60	23-Jan-10	18:39		15.0		44.1099	44.0245	1.31
			26-Jan-10	5:22				44.1105	44.0638	1.31
		2004 VZ75	30-Oct-09	2:47		40.0		41.2635	40.9819	1.38
			2-Nov-09	16:52				41.2617	40.9228	1.35
		2005 EF298	15-Jun-10	22:05		30.0		40.7405	40.2296	1.23
			19-Jun-10	14:03				40.7400	40.2840	1.27
303712		2005 PR21	12-Jan-10	2:46		43.3		41.0656	40.9459	1.41
			16-Jan-10	21:40				41.0666	41.0283	1.41
145452		2005 RN43	18-Dec-10	9:47	10:07	15.0		40.6813	40.1723	1.25
			21-Dec-10	19:14	19:34			40.6812	40.2222	1.29
		2006 HW122	16-Sep-09	1:50		23.3		43.9516	43.7738	1.32
			20-Sep-09	15:47				43.9523	43.8509	1.33
		2007 TY430	30-Jan-10	20:33		15.0		29.1760	28.6759	1.74
			3-Feb-10	12:44				29.1751	28.7311	1.79

^a - Time is given at the start of the observation.

^b - Integration time for each channel.

^c - Heliocentric distance r , observer distance Δ , and phase angle α are given in Spitzer-centered coordinates.

IRAC data frames have been pre-processed by the Spitzer Science Center (SSC) automated pipeline for dark subtraction, flat fielding, and flux calibrations. Corrections for IRAC specific artifacts such as column pulldown, muxbleeding, array pulldown, stray light contamination, etc., are done for individual frames if necessary. Each object is observed twice, initially and after the object has moved relative to the same sky field. A background frame for each observation is made by averaging the dithered frames from the other date, omitting outliers, and shifting them to a common pointing. The background is subtracted from each data frame leaving a single positive source, the object, and a negative ‘shadow’, the object on the other date (fig. 2.1). A visual inspection of each frame, the average frame, and the background subtracted frame for each observation was conducted to assess success of the observation. If objects were not discernible by eye in the observation, an upper limit calculated by the background flux is presented. The background flux is the mean of 50 randomly selected pixels, ignoring outliers $\pm 2\sigma$, within a radius of 50 pixels of the location of the object predicted by its ephemeris. Corrections (available from the SSC) for variation

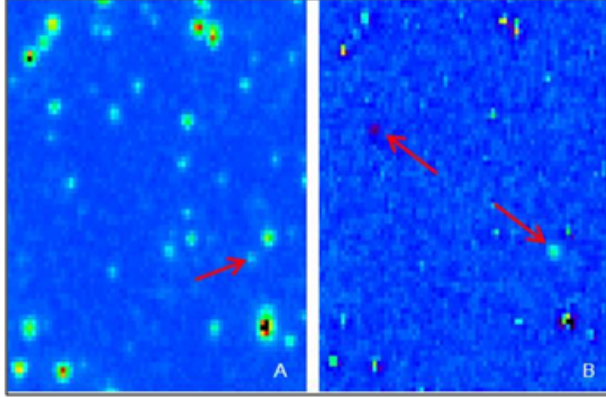


Figure 2.1: Background subtraction from repeated IRAC observations. Both images show the same FOV. Before background correction (A) the FOV is bright and confusing. After background subtraction (B) the object and its negative are easily identifiable. Red arrows indicate the object and shadow.

in the pixel solid angle and array location dependent photometric variations are applied to the frames.

To calculate the flux from the object, aperture photometry is performed as outlined in the IRAC Instrument Handbook². A computer generated aperture is placed around the object and the background flux per pixel is calculated within an annulus. The background is subtracted from the flux in the aperture and the total flux in the aperture is calculated. Four combinations of aperture radius and background annulus are used: a 2 pixel radius aperture with 2-6 pixel and 10-20 pixel background annulus, and a 3 pixel radius aperture with 3-7 and 10-20 pixel annulus (Emery et al., 2007). Aperture corrections for each combination are given in the IRAC Instrument Handbook. Assuming a solar spectral slope through each passband (Smith and Gottlieb, 1974), color corrections are calculated for each broad-band channel. All aperture/annulus combinations and all frames in an observation are averaged together for each channel and recorded as final fluxes. Uncertainties of 1σ are reported. The uncertainties account for photon counting statistics, deviation among the dithered frames, and deviation among the aperture/annulus combinations. The absolute calibration of all IRAC channels is accurate to $\sim 3\%$ (Reach et al., 2005). The pixel location of the object in each frame is calculated from known ephemerides obtained from the JPL Solar System Dynamics group (Giorgini et al., 1996). Visual confirmation of the object location is required

²<http://irsa.ipac.caltech.edu/data/SPITZER/docs/spitzermission/>

to report the calculated final flux (fig. 2.1). If the object is not discernible in a channel or the uncertainty overlaps zero, the upper limit of the background flux in the channel is reported.

To support the *Spitzer* observations, NIR photometric data from ground based and *Hubble Space Telescope (HST)* observations have been compiled. Spectrophotometric measurements from ground based telescopes to provide a continuum for absorption identification at $\lambda > 2.5 \mu\text{m}$ and broaden the lever for determining the composition in wavelength space. Establishing a continuum is very important; an absorption feature cannot be identified if there is no datum from which to measure. To properly identify absorption, the K-band ($\sim 2.2 \mu\text{m}$) is critical for establishing a reflectance continuum and the J- and H-bands (~ 1.25 and $\sim 1.65 \mu\text{m}$, respectively) indicate the shape of the spectrum. This combination of data constrains the presence of ices and allows for first order approximations of surface compositions on cold classical KBOs. Published *HST* vis-NIR data are also available in platform specific filters, some of which have been transformed into JHK band values. For objects without published NIR photometry, published visible data are used to correlate visible slopes for approximating K-band values. Appendix B contains tables of published photometry used for this study.

3. Results

3.1 *Spitzer* IRAC results

The measured fluxes in the IRAC channels are converted into geometric albedos so they can be combined with the ground-based data. The geometric albedo, p_λ , at wavelength λ is given by

$$p_\lambda = \frac{F_\lambda r_{AU}^2 \Delta^2}{F_{\odot,\lambda} \Phi R^2}, \quad (3.1)$$

where F_λ is the flux, $F_{\odot,\lambda}$ is the solar flux density, r_{AU} and Δ are the heliocentric and Spitzer-centric distances, R is the object radius, Φ is a correction for the phase angle of the observation. If the linear phase coefficient for an object is available in the literature, that value is used to calculate the phase correction. Otherwise, the published average of analyzed KBOs from Rabinowitz et al. (2007) is used to approximate the correction. The radii of several cold classical KBOs observed by IRAC have been published. However, if an observed radius is not available, one is calculated by

$$R = \frac{1}{2} 1346 p_v^{-1/2} 10^{-H_v/5}, \quad (3.2)$$

where H_v is the absolute magnitude, and p_v is the V-band geometric albedo. IRAC fluxes for ch1 and ch2 and corresponding albedos are presented in appendix A.

Visible albedos and radii used to calculate IRAC channel albedo are also presented in appendix A. For objects without available p_v , the average KBO value from Stansberry et al. (2008) is used. To combine the ground-based photometric and IRAC data, the respective albedos must be scaled similarly. The ratio of ground-based albedo and IRAC albedo is independent of the choice of R and p_v . As long as the visible albedo used to scale the

ground-based data is consistent with the radius of the object used in the IRAC albedo calculation, the identification of an absorption will be accurate.

3.2 Cold classical classification

In *The Solar System Beyond Neptune* (SSBN07), Gladman et al. (2008) distinguish the hot and cold classical KBOs by inclination distribution. The inclination of hot classical objects has Gaussian distribution peaking at $\sim 15^\circ$. The division based on inclination is debated, with lines most often drawn at 5° or 12° ; the cold objects are the lower inclination objects. The inclination distinction may not have a dynamical basis (Kavelaars et al., 2008), and inclination distribution is not the only way the classical population has been separated. Petit et al. (2011) suggest perihelion coupled with semi-major axis, a , provides a better division between hot and cold populations. Objects with $42.5 < a < 47.2$ AU and $q \leq 40$ AU are defined as cold classical objects. The objects with $a < 40$ AU and $a > 47.2$ AU are inner and outer hot objects, respectively. The objects in the $40 < q < 42.5$ AU region are a mixture of hot and cold objects, and the fraction of cold objects increases closer to $a = 42.5$ AU. Five objects observed in the IRAC program: 48639 1995 TL8, 19521 Chaos, 20000 Varuna, 50000 Quaoar, and 142452 2005 RN43, fall within these orbital definitions and are included as cold classical objects here.

Sheppard (2012) suggests from color of objects in the MMRs located in the classical population (7:4 and 5:3) that these object may be captured cold classicals. The objects in the 7:4 and 5:3 resonances are very red, similar to the extremely red slopes of more traditionally classified cold classical objects. 1999 CD158 and 126154 2001 YH140 are in the 7:4 and 5:3 MMRs, respectively. Both have been observed in the IRAC program and are included in this study. If the objects in the 7:4 and 5:3 are captured cold classicals, one would expect to see similar binary populations as well. However Noll et al. (2012) do not see similar distributions of binaries in the MMRs and the cold classical population. For completeness, the present work includes objects fitting the cold classification according to the Petit and Sheppard schemes.

3.3 Vis-NIR data

Vis-NIR data are essential to constrain the nature of the absorption and the composition of the surface.

- 33 out of the 46 objects in this survey have at least some published standard vis-NIR (BVRIJHK) photometry.
- 9 objects have all (B-V, V-R, V-I, V-J, V-H, V-K) colors, or photometric data to calculate the colors, published.
- 14 objects have V-K colors available.

See appendix B for a summary of published photometry and appendix C for photometric plots.

138537 2002 OK67 is an example of an object for which photometry has been published for bands through the vis-NIR (fig. 3.1). The red and green circles are the IRAC observations, those in red occurring first. The green arrow in IRAC ch1 is an upper limit because the error overlaps zero. Eight other objects have full vis-NIR data available 66652 Borasisi, 79360 Sila-Nunam, 134860 2000 OJ67, 1999 CD158, 2000 Varuna, 50000 Quaoar, 19521 Chaos, and 48639 1995 TL8 (fig. C.1, fig. C.7, and fig. C.8). 145452 2005 RN43 (bottom, fig. C.8) is only missing V-R color data, which does not affect our analysis.

Trujillo et al. (2011) observed KBOs using custom filters manufactured to measure H₂O and CH₄ absorptions at 2.03 and 2.28 μm respectively. The four objects that overlap our study and theirs are 2000 CN105, 119951 2002 KX14, 50000 Quaoar, and 120347 Salacia. Sheppard (2012) present data using the same filters for 2007 TY430. See table B.2 for colors from Trujillo et al. (2011) and transformations to J-K. The published K-band for Quaoar (DeMeo et al., 2009) produces a lower albedo than the transformation of H₂O and CH₄ filters; the H₂O and CH₄ bands are plotted on the Quaoar photometry plot for comparison (fig. C.9, bottom plot).

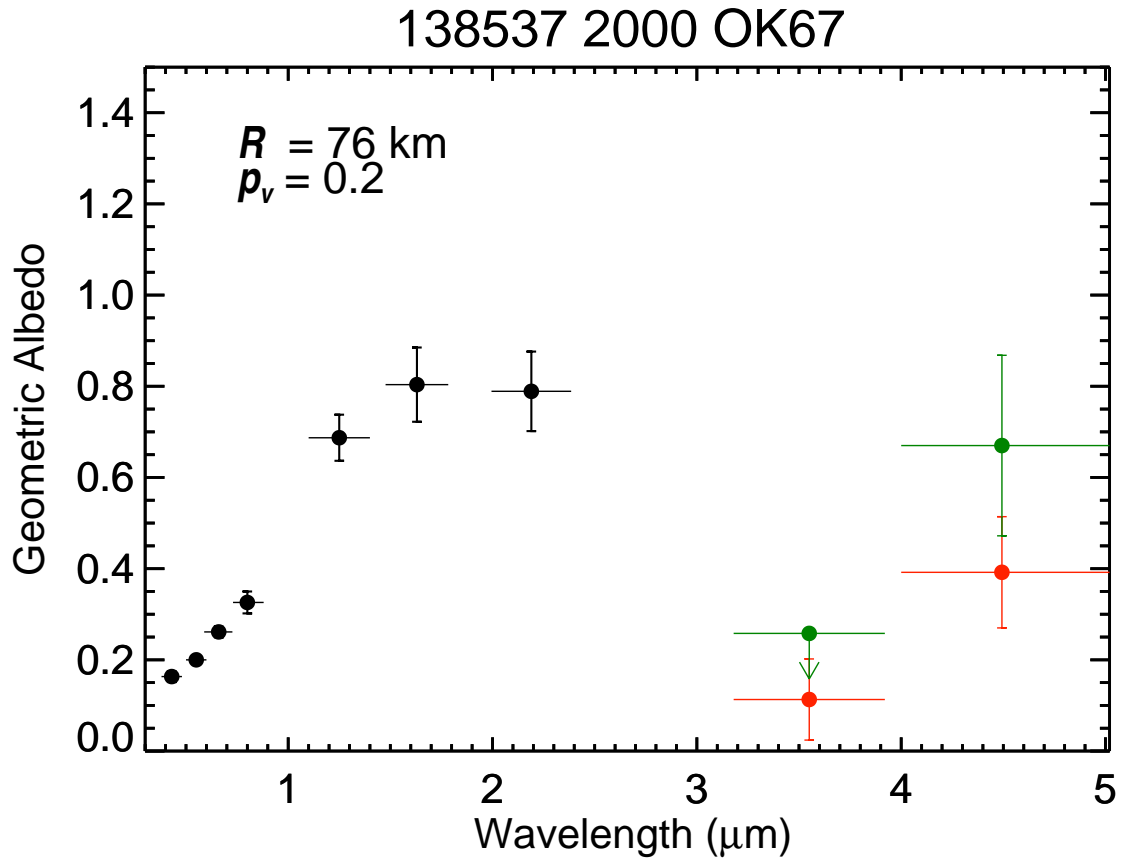


Figure 3.1: Spectral plot for 138537 2002 OK67. Black circles are published visible photometry from Doressoundiram et al. (2002), and NIR photometry from Delsanti et al. (2004). Observation dates were 13-Jan-10 (red circles) and 17-Jan-10 (green circles). The green arrow is an upper limit because the error bar overlaps zero.

4. Analysis

4.1 Absorption at IRAC wavelengths

The first order test for ices is to look for absorptions in the IRAC channel wavelengths. The majority of this cold classical sample only has ch1 observations available because of the faintness of the objects in ch2. Ch1 is sensitive to CH₄ and H₂O ices and, interestingly, organics such as Titan tholins. See fig. 4.3 for spectra of volatile ices and tholins. The featureless spectra of silicates at these wavelengths are distinct from those of ices or organics. Assessment of an absorption in ch1 is straight-forward for objects with published K-band photometric data, such as 138537 2002 OK67 (fig. 3.1). A negative K-ch1 color is an indication of an absorption at wavelengths that include IRAC ch1. The K-ch1 color for each observation is calculated by

$$K - ch1 = 2.5 \log \frac{p_{ch1}}{p_K}, \quad (4.1)$$

where p_{ch1} and p_K are the respective albedos in each band. The calculated IRAC albedos of the two observations for each object are averaged together for the K-ch1 color of the object. K-ch1 colors for all objects in our sample are presented in fig. 4.2 and table 4.3.

To produce a continuum from which to measure K-ch1 for objects without published K-band data, we assume the average of objects within this sample that have published data for the shortest wavelength gap. For example, Santos-Sanz et al. (2009) published BVRI photometry for 2002 VT130 (fig. 4.1). No JHK photometry for 2002 VT130 is available at this time. The average I-K, the shortest wavelength gap, of the objects with similar visible slope and available I-K and is used to produce a K band albedo for 2002 VT130. For objects with no available photometry, the average V-K color of the ten objects with K-band

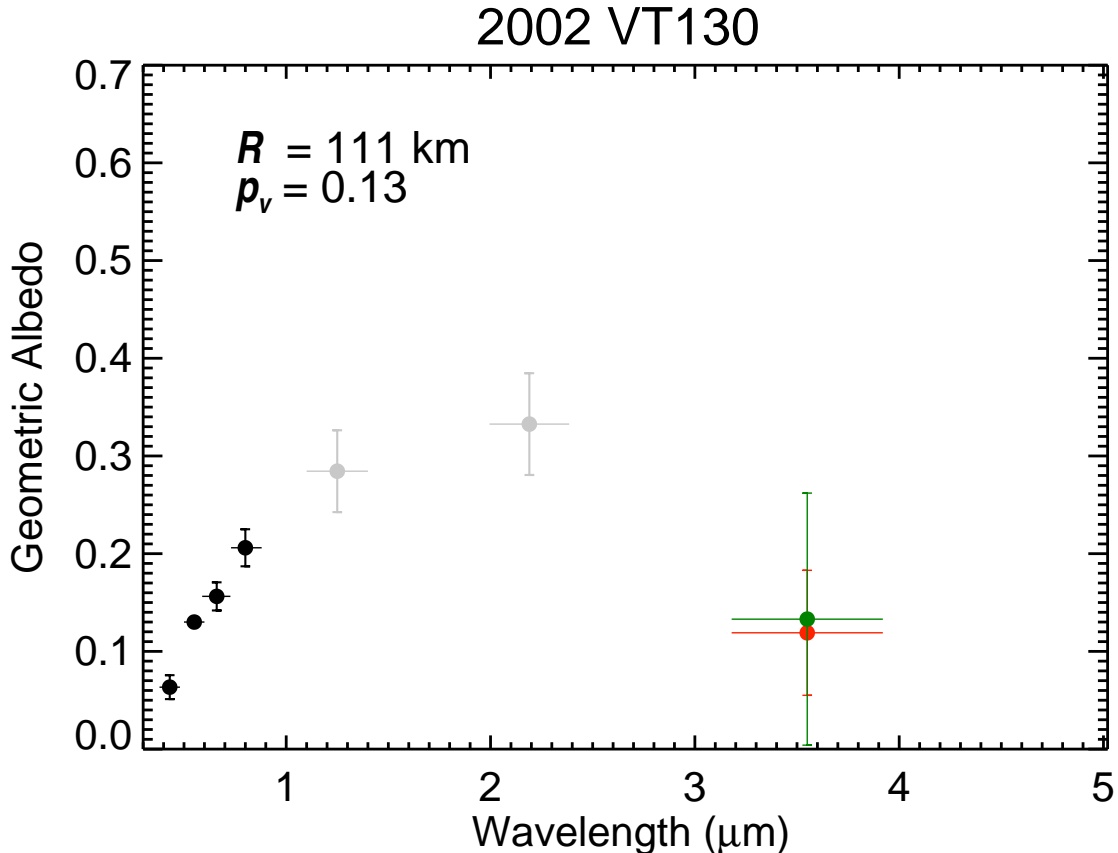


Figure 4.1: Spectral plot of 2002 VT130. Published photometric data, black circles, are from Santos-Sanz et al. (2009). No JHK data are available for this object. Gray circles are average J and K-band albedo from 10 sample objects with JHK data. Uncertainties on the estimated J- and K-band albedos are propagated from the averaged colors. Red and green circles are IRAC ch1 observations.

data is used with the p_v of the object to assess the possibility of an absorption at IRAC wavelengths. See table 4.1 for sample averaged colors. In table A.1, V-K colors indicated with a superscript a are average colors.

HST vis-NIR photometry is useful as a continuum to compare with the *SST*/IRAC data for several objects. Twenty-three objects in this study have *HST* vis-NIR photometry (table B.3) published by Benecchi et al. (2009, 2011) and Fraser and Brown (2012). For objects with some published standard filter photometric data but no K-band data, *HST* data provide a visual guide to judge how well the sample averaged color fits the spectral shape for a particular object.

Table 4.1: Average photometric colors.

Color	Average			No.	Color	Average			No.
B-V	0.99	+/-	0.09	27	V-J	1.95	+/-	0.07	12
V-R	0.61	+/-	0.07	29	V-H	2.40	+/-	0.16	13
V-I	1.16	+/-	0.09	27	V-K	2.49	+/-	0.11	10
R-J	1.39	+/-	0.11	12	I-K	1.26	+/-	0.14	10
I-J	0.74	+/-	0.12	13	J-K	0.46	+/-	0.13	10
R-K	1.91	+/-	0.12	9	H-K	0.04	+/-	0.12	10

The oblateness of the objects and related lightcurves could affect interpretation of the results and identification of absorptions. The average KBO lightcurve amplitude, peak-to-peak, is 0.24 with a standard deviation of 0.22 mag (Sheppard et al., 2008), therefore $\sim 15\%$ of our objects may have amplitudes of > 0.46 mag. There is only a 22% chance of any two observations varying more than half of the amplitude. We would expect this variation to affect $< 4\%$ of our sample, or two objects. However, even given the aforementioned amplitude variation, we will still be able to identify absorptions.

As indicated above, the quality of the vis-NIR and IRAC data for the objects studied here is varied, and the interpretation is affected by that variation in quality. Each object is therefore assigned to a data quality group:

- 11 objects have secure detections in ch1 and published K-band data.
- 21 objects have secure detections in ch1, but no published K-band data (i.e., some assumptions regarding NIR colors are required to establish the continuum and the average V-K color is used).
- 13 objects were not detected in ch1, in which case upper limits on the ch1 albedo are established.

Of the 46 observed cold classical Kuiper Belt objects, 14 objects have available K-band data, which provides a lever to assess presence of an absorption at $\lambda > 2.5 \mu\text{m}$. The K-ch1 color of the eleven objects with both published K-band data and secure IRAC ch1 observations show presence of an absorption (red and blue diamonds, fig. 4.2). Eight of those eleven objects show unambiguous absorptions; the error in the K-ch1 color does not overlap zero. For objects without K-band data, the average of objects with a similar visible

Table 4.2: Objects with negative K-ch1 color.

Data quality group	No. obj	K-ch1 + σ		K-ch1 < 0	fraction
		< 0	fraction		
IRAC ch1 and vis-NIR	11	8	0.73	11	1.00
no K-band data	21	11	0.52	14	0.67
ch1 upper limit	13	9	0.69		
All	45	29	0.64	35	0.78

slope, in the case of objects with visible photometry, or all objects in our sample was used to assess possible absorptions (black diamonds, fig. 4.2). Absorptions are suggested on 14 out of 21 objects assessed with sample averaged photometry. Objects that only have upper limits for observations with IRAC, 9 of 13, also display absorptions (maroon arrows, fig. 4.2). Taken together, 78% of these cold classical objects show absorptions (table 4.2). Seven objects have ch1 albedos higher than the sample averaged K-band albedo and therefore a positive k-ch1 color. It is important to note that none of these seven objects has published K-band photometry and use sample averaged K-band data.

An interesting feature of fig. 4.2 is the change in slope of roughly thirds of the plot. The data at higher K-ch1 end are assessed with sample averaged data and not much can be said about the steeper slope. The objects on the middle, flatter slope are likely a mixture of silicates and ices leading to more moderate absorptions. Objects with stronger absorptions (left of plot) have a steep slope. These deep absorptions may be from the combination of organics embedded in ices. It will be interesting to see if these inflections are seen in the Kuiper Belt as a whole or are unique to the cold classical objects.

4.2 Surface composition analysis

Visible and near-infrared spectroscopy and photometry of the KBOs and Centaurs have revealed a surprisingly varied range of colors and spectral reflectances. Some objects show no diagnostic spectral bands while spectra of others show signatures of various surface components: ices of H₂O, N₂, CH₄, light hydrocarbons (e.g. CH₃OH). The diversity in these spectra suggests the bulk compositions of KBOs are equally varied.

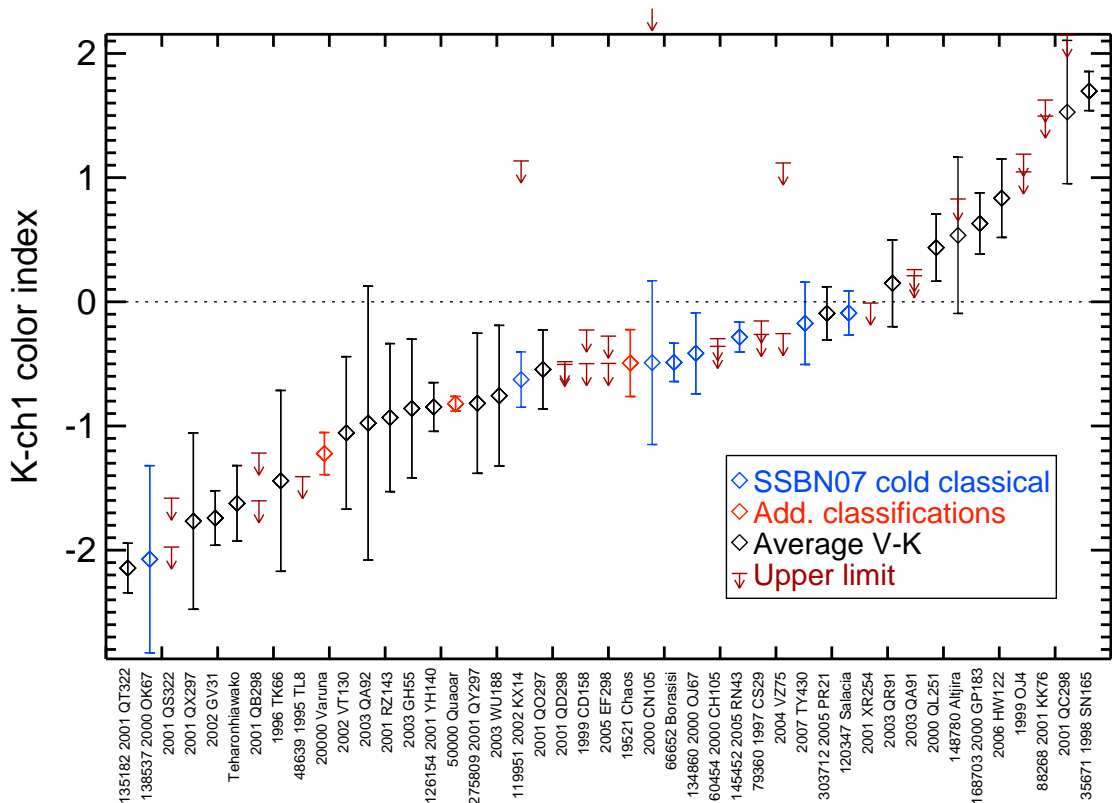


Figure 4.2: K-ch1 color indices for cold classical KBOs, sorted by color index. Negative K-ch1 color indicates an absorption at $\lambda > 2.5 \mu\text{m}$. Blue and red diamonds are objects with published K-band data. Black diamonds represent objects with sample averaged K-band data. An upper limit (maroon arrow) in ch1 suggests an absorption.

The visible spectra of KBOs are generally featureless, but have a large variation in gradient from neutral to very red. The reddest objects, those whose reflectance increases steeply with wavelength, are interpreted to indicate the presence of some organic material on their surfaces. The visible range can also be used to identify aqueously altered minerals such as phyllosilicates. Although potential silicate bands ($\sim 0.7 \mu\text{m}$) have been reported on a few KBOs, none of the features have yet been confirmed (Vilas and Gaffey, 1989; Jewitt and Luu, 2001). The NIR (1-2.5 μm) is more diagnostic for identifying the presence of many ices. Absorption features due to H_2O , CH_4 , CO , N_2 , CH_3OH , NH_3 , and C_2H_6 have been reported in NIR spectra of KBOs, and CO_2 has been detected on satellites of Uranus and

Neptune (Cruikshank and Silvaggio, 1979; Brown et al., 1997; Luu and Jewitt, 1998; Brown et al., 1999).

Vis and NIR spectra have been combined to further constrain the surface composition of the brightest KBOs and Centaurs. The radiative transfer models of Hapke (1993) are used to interpret these spectra by using different mixture types, mixing ratios, and material parameters of optically measured materials. The red slopes are reproduced well by inclusion of organic compounds like tholins or kerogens on the surface. Flat slopes are well modeled by large fractions of amorphous carbon. Silicates are also present on some surfaces. For example, Cruikshank et al. (1998) use olivine to significantly improve the model fit of spectra of Centaur 5145 Pholus. Many objects have moderate to deep 1.5 and 2.0 μm absorptions due to water ice. The objects with the greatest water absorption depths are associated with the Haumea collisional family (Brown et al., 2007). The largest KBOs, Eris, Pluto, and Makemake, have more complex spectra dominated by methane absorptions (Brown, 2008). Some objects show both CH_4 and N_2 , however others have clear indications of pure CH_4 ice. Methanol, or a photolytic product of methanol, has been identified on 55628 2002 VE95 by Barucci et al. (2006). Featureless objects exhibit spectra with no identifiable features. The featureless objects range in color from gray to some of the reddest objects in the Solar System. Barucci et al. (2008) define several broad spectral categories for KBOs:

1. methane-dominated spectra,
2. water-ice-dominated spectra,
3. water-ice spectra with the presence of methanol-like features, and
4. featureless spectra.

In an independent analysis of published spectra, Brown et al. (2011) describe essentially the same basic spectral groups. However, they divide the water-ice dominated groups by depth of water band and spectral slope of the non-ice component.

At longer wavelengths, most ices are spectrally distinct from each other (fig. 4.3). CH_4 has a strong absorption centered at 3.3 μm . H_2O has an absorption around 3.0 μm and a broader absorption centered around 4.3 μm . CO_2 has an absorption at 4.25 μm . Organics,

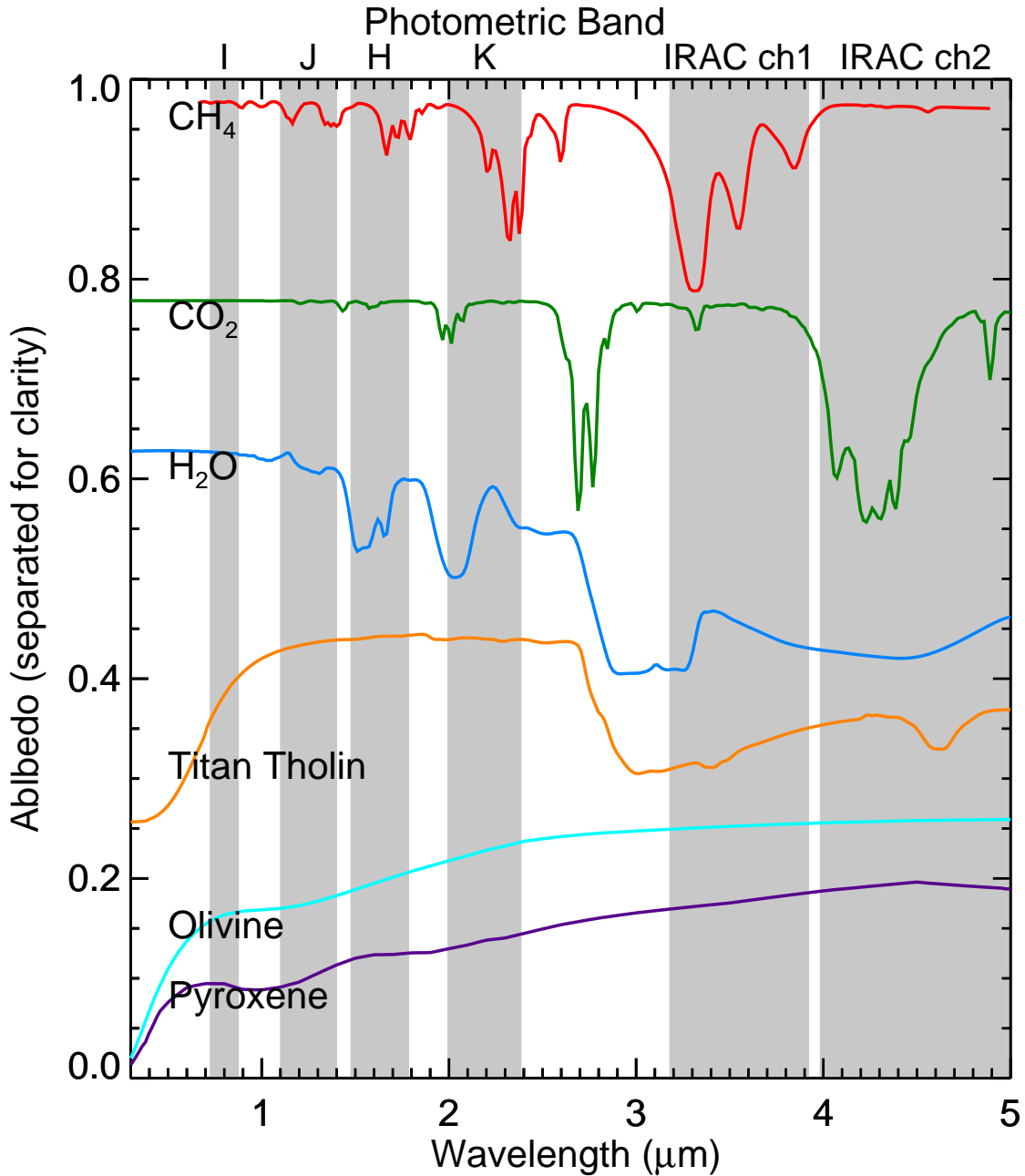


Figure 4.3: Absorption spectra of CH₄, CO₂, and H₂O ices at 40K, organic Titan tholin, and amorphous silicates olivine and pyroxene, separated for clarity. Standard photometric filters and IRAC channels (grey bars) are plotted for reference.

represented here by Titan tholin, have a broad absorption at about 3.2 μm . While organics and H₂O have similar absorptions at these longer wavelengths, their visible spectra are very different. Anhydrous silicates, such as olivine and pyroxene likely in an amorphous state,

expected on objects that have undergone little thermal evolution have no absorptions at $\lambda > 2.5 \mu\text{m}$. It is important to note these materials are all spectrally distinct, even at the coarser broadband wavelength resolution of NIR and IRAC photometry (grey bars, fig. 4.3).

Observation of these longer wavelength absorptions is difficult from the ground because of high (and rapidly varying) background emission and absorption of incoming light by water vapor in the Earth's atmosphere. *SST*, in an Earth-trailing orbit, avoids these problems allowing for investigation of diagnostic absorptions of materials observed or hypothesized on KBO surfaces at $\lambda > 2.5 \mu\text{m}$ for a large number of KBOs.

The utility of *SST*/IRAC photometry for identifying the spectrally dominant materials on the surfaces of KBOs can be illustrated by considering the spectra in fig. 4.3. The strong absorption of CH_4 centered at $3.3 \mu\text{m}$ falls well into IRAC ch1 at $3.6 \mu\text{m}$ and there are no appreciable absorptions in the $4.5 \mu\text{m}$ ch2. Therefore the reflectance of methane in ch2 will be higher than in ch1. Conversely, the CO_2 absorption at $4.25 \mu\text{m}$ will cause the ch2 albedo to be lower than ch1. Water has a broad absorption at $3.0 \mu\text{m}$ that extends into ch1, creating similar albedos in ch1 and ch2. The volatile ices have lower reflectance in ch1 than K-band. Silicates tend to have similar albedos at the K-band and ch1 wavelengths. Tholins have a higher ch1 albedo than K-band. The band differences, called here color indices, are compared on a color-color plot. K-ch1 and ch1-ch2 colors are presented in table 4.3. Colors reported without errors are upper limits.

Table 4.3: IRAC color indices for cold classical objects.

Object	K-ch1		ch1-ch2		
135182 2001 QT322	-2.14	+/-	0.20		
138537 2000 OK67	-2.07	+/-	0.75	1.60	+/- 0.90
2001 QS322	<-1.97				
2001 QX297	-1.77	+/-	0.71		
2002 GV31	-1.74	+/-	0.22		
Teharonhiawako	-1.62	+/-	0.30		
2001 QB298	<-1.60				
1996 TK66	-1.44	+/-	0.73		
48639 1995 TL8	<-1.41				
20000 Varuna	-1.22	+/-	0.17	0.21	+/- 0.27
2002 VT130	-1.06	+/-	0.61		
2003 QA92	-0.98	+/-	1.10		
2001 RZ143	-0.93	+/-	0.60		

Continued on next page

Table 4.3: continued

KBO	K-ch1		ch1-ch2			
2003 GH55	-0.86	+/-	0.56			
126154 2001 YH140	-0.85	+/-	0.20			
50000 Quaoar	-0.82	+/-	0.06	-0.22	+/-	0.10
275809 2001 QY297	-0.82	+/-	0.56			
2003 WU188	-0.76	+/-	0.57			
119951 2002 KX14	-0.63	+/-	0.22	-0.63	+/-	0.22
2001 QO297	-0.54	+/-	0.32			
2001 QD298	<-0.50					
1999 CD158	<-0.50					
2005 EF298	<-0.50					
19521 Chaos	-0.49	+/-	0.27	0.18	+/-	0.40
2000 CN105	-0.49	+/-	0.66			
66652 Borasisi	-0.49	+/-	0.15	0.81	+/-	0.26
134860 2000 OJ67	-0.41	+/-	0.33			
60454 2000 CH105	<-0.36					
145452 2005 RN43	-0.28	+/-	0.12			
79360 1997 CS29	<-0.26					
2004 VZ75	<-0.26					
2007 TY430	-0.17	+/-	0.33			
303712 2005 PR21	-0.09	+/-	0.21			
120347 Salacia	-0.09	+/-	0.18			
2001 XR254	<-0.01					
2003 QR91	0.15	+/-	0.35			
2003 QA91	<0.21					
2000 QL251	0.44	+/-	0.27			
148780 Altjira	0.54	+/-	0.63			
168703 2000 GP183	0.63	+/-	0.25			
2006 HW122	0.83	+/-	0.32			
1999 OJ4	<1.05					
88268 2001 KK76	<1.50					
2001 QC298	1.53	+/-	0.58			
35671 1998 SN165	1.70	+/-	0.16			

The distinct photometric behaviors of these materials are evident on a K-ch1, ch1-ch2 color-color plot (fig. 4.4). The various ices, organics, and silicates occupy different regions of color space. The material fields are ranges of results for the materials modeled across a range of grain sizes. K-band and IRAC colors of the cold classical KBOs can be analyzed in this context as well. The six objects with secure observations in both IRAC ch1 and ch2 and published K-band photometric measurements, 19521 Chaos, 20000 Varuna, 50000 Quaoar,

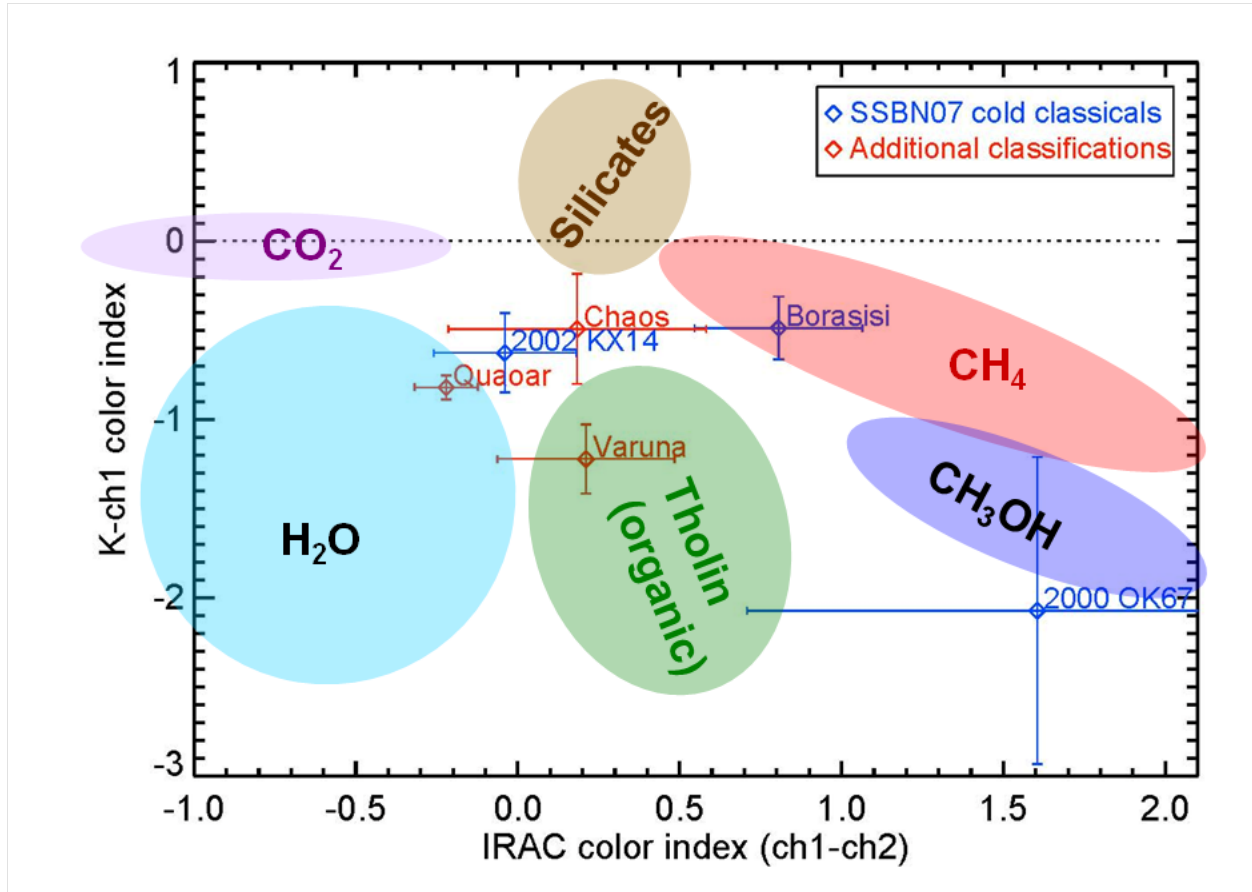


Figure 4.4: K-ch1, IRAC color index color-color plot of cold classical objects. Fields are plotted by modeling materials at different grain sizes.

66652 Borasisi, 119951 2002 KX14, and 138537 2000 OK67, are plotted in K-ch1 ch1-ch2 color space on fig. 4.4. The fields for each material are produced by modeling the materials at different grain sizes and encircling the results. If the object plots within a particular field, it is spectrally dominated by that material in . Surface materials on these objects are analyzed below and summarized in table 4.4.

4.2.1 19521 Chaos

Although Chaos plots between the materials fields in fig. 4.4, the negative K-ch1 color clearly shows an absorption in ch1. This is the first clear detection of ices on Chaos. Barkume et al. (2008) notice a broad dip (1.7-2.0 μm) in their NIR spectra of Chaos, but attribute the dip to poor atmospheric correction. The surface is most likely a mixture of H_2O and CH_4

with hydrocarbon and organic components, although other materials cannot be completely dismissed as possibilities.

4.2.2 20000 Varuna

Licandro et al. (2001) identified 1.5 and 2.0 μm water bands in Varuna's spectrum and a very red color related to chemical evolution of the surface materials. However, Barkume et al. (2008) did not detect water ice on the surface. According to the taxonomy of Barucci et al. (2005), Varuna is an intermediately sloped, or IR, object; they suggest the IR taxon may have hydrous silicates on their surfaces. The relatively deep K-ch1 color indicates an ice or organic absorption. These features, along with the red V-K color (fig. 4.5), indicate ices with tholin or other red organic compounds. Varunas surface is consistent a mixture ices and organic material.

4.2.3 50000 Quaoar

Jewitt and Luu (2004) first reported water ice on the surface of Quaoar. Schaller and Brown (2007a) identified CH_4 , although the significant amount of H_2O on the surface dominates the gross composition seen here. Guilbert et al. (2009) also find small amounts of methane ice. Dalle Ore et al. (2009) modeled the surface of Quaoar with 36-53% amorphous and crystalline water ice. Their range in water ice fraction comes from addition of N_2 from 0-20%. Quaoar plots well into the H_2O field, with a negative K-ch1 and positive ch1-ch2, on the color-color plot (fig. 4.4). This confirms the presence of water ice on Quaoar's surface.

4.2.4 66652 Borasisi

Barkume et al. (2008) were unable to detect specific ice signatures on Borasisis surface, although they notice a broad dip (1.7-2.0 μm) near the 1.8 μm telluric water line in their NIR spectra which they attribute to poor atmospheric correction. The K-ch1 color is unambiguously negative and indicates a clear absorption. Therefore, we report the first clear indication of ices or organics on the surface of Borasisi. The consistency of this method with previous observations of Quaoar and Varuna lend credence the method of comparing

Table 4.4: Observed ices

No.	Name/Designation	Observed Surface Materials
19521	Chaos	mixture
20000	Varuna	organics
50000	Quaoar	H ₂ O
66652	Borasisi	CH ₄
119951	2002 KX14	mixture, H ₂ O
138537	2000 OK67	CH ₃ OH

the object in color-color space with modeled material fields. The ch1-ch2 color of Borasisi is consistent with methane. The red V-K of Borasisi indicates organics. Borasisi surface is likely organic material interspersed in methane ice. Other combinations materials may produce a similar result, for example Borasisi may be plotted on a line connecting methanol and silicates. However, the spectra of the materials of interest do not combine linearly and compositional analysis becomes much more complicated.

4.2.5 119951 2002 KX14

Barkume et al. (2008) did not detect ices on the surface of 2002 KX14, but did notice a broad dip (1.7-2.0 μm) that they attributed to poor telluric correction, as with Chaos and Borasisi. A negative K-ch1 shows an absorption, the first detection of ices or organics on 2002 KX14 (fig. 4.4). The ch1-ch2 color is slightly positive, an indication of water ice. The slight increase in reflectance from ch1 to ch2 may also an indication of the presence of silicates. The surface of 2002 KX14 is likely a mixture of materials with an appreciable fraction of water ice, organics produced by the chemical evolution of ices, and silicates.

4.2.6 138537 2000 OK67

Interestingly, 2000 OK67 did not initially fit into a taxa set forth by Barucci et al. (2005). However, Fulchignoni et al. (2008) classify is as RR. 2000 OK67 is a rather red V-K object with a pronounced absorption in ch2 (fig. 4.4). Although 2000 OK67 plots just outside the methanol field, its surface likely contains methanol or other simple hydrocarbon molecules. This is the first detection of ices on 2000 OK67.

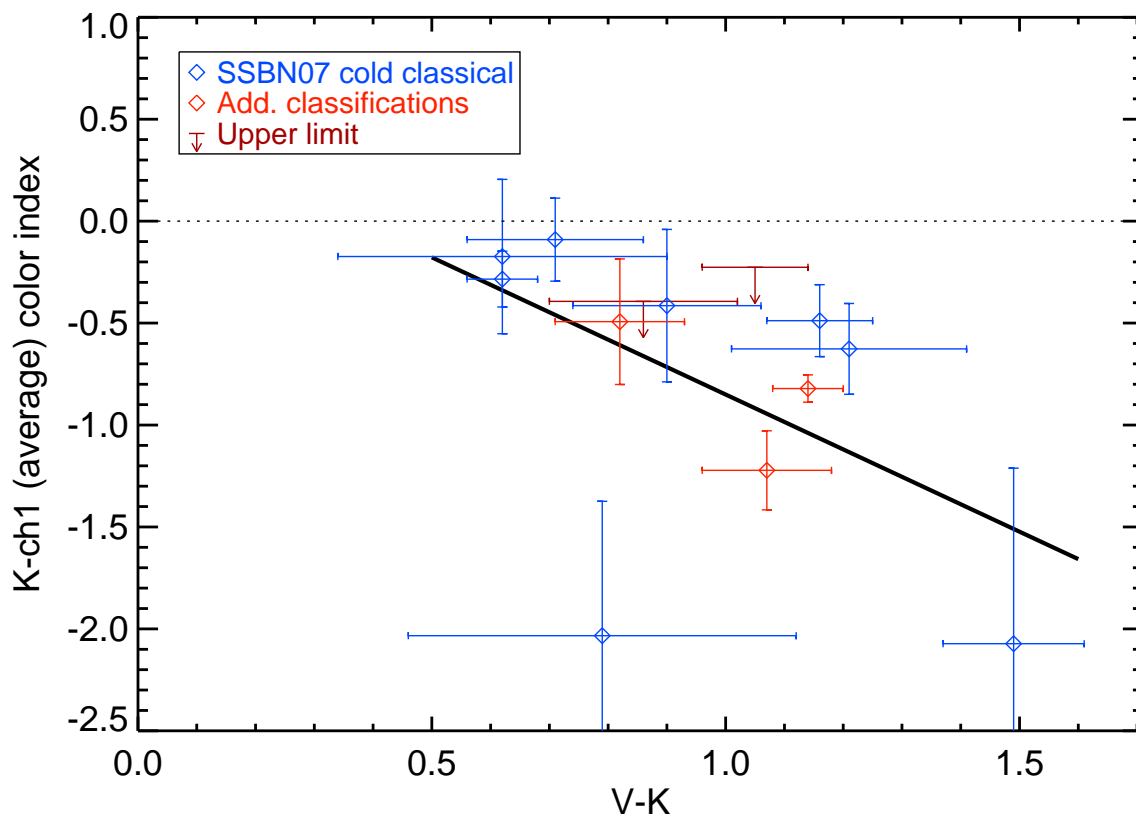


Figure 4.5: K-ch1 (average) vs. V-K color indices. Objects traditionally classified as cold classical are blue diamonds, objects fitting in Petit et al. (2011) or Sheppard (2012) classifications are red diamonds, objects with upper limits and published photometry are maroon arrows. Of these 10 objects, 9 have absorptions $\lambda > 2.5 \mu\text{m}$ indicating volatiles present. The new IRAC data reveal that objects with steeper vis-NIR spectral slopes (higher V-K on this plot) have more pronounced absorptions. The black solid line is a least-squares best fit of the data.

It would be useful to perform the above analysis on our entire sample. Unfortunately, most of the cold classical objects are too faint for observation in IRAC ch2 ($4.5 \mu\text{m}$). Figure 4.5 is a K-ch1 V-K color-color plot of objects with published K-band data. Objects with steeper or redder slopes have higher V-K colors. The more negative a K-ch1 color, in this plot averaged between the two observations, the more pronounced the absorption is. The black best-fit line shows a correlation between redder slopes and more pronounced absorptions. This correlation suggests we are seeing red sloped organics on the surfaces of these cold

classical objects. There is ongoing debate whether the organic material was incorporated into objects or formed by chemical evolution (Dalle Ore et al., 2011).

4.3 Correlations with object characteristics

Correlations among spectral (compositional), physical, and orbital properties of small bodies have the potential to shed light on the evolution of those bodies. The colors available in this data set (B-V, V-R, V-I, V-J, V-H, V-K, K-ch1, ch1-ch2) have been paired with orbital parameters (a , e , i , q , Q) and physical characteristics (p_v , R , H_v) to assess correlations of colors and object orbit and properties. Cold classical objects are expected to have formed where they are, or at > 30 AU (Levison et al., 2008; Batygin et al., 2011), far enough from the Sun, that volatiles condense during formation. Even though the cold classical belt is relatively narrow ($42.5 < a < 47.5$ AU), a chemical gradient across the region is reasonable to expect (Brown et al., 2011). Since these bodies are thought to have undergone little to no thermal evolution or processing, this gradient is expected to be retained as volatile composition across the region. Band differences with respect to orbital parameters, such as semi-major axis, inclination, eccentricity, and perihelion should be correlated in some way because of chemical gradients of formation. Additionally, if the cold classicals have undergone thermal processing in some systematic way, the signature of that process may be left.

One of the primary spectral/orbital pairs of interest is the orbital distance from the Sun and depth of absorption. The most straight-forward proxies for distance and depth are semi-major axis and K-ch1 color. No correlation was seen between these quantities (fig. 4.6, upper left). Other orbital parameters and colors were also searched, but no combination showed correlation. To illustrate the results, parametric plots for K-ch1 color are shown in fig. 4.6. These data include sample averaged K-band values. The distribution of surface volatiles for the newly collected KBO data combined with previously published data for cold classical KBOs does not correlate to any orbital characteristics. A chemical gradient is not found across the cold classical population. There is no evidence for thermal processing in these data.

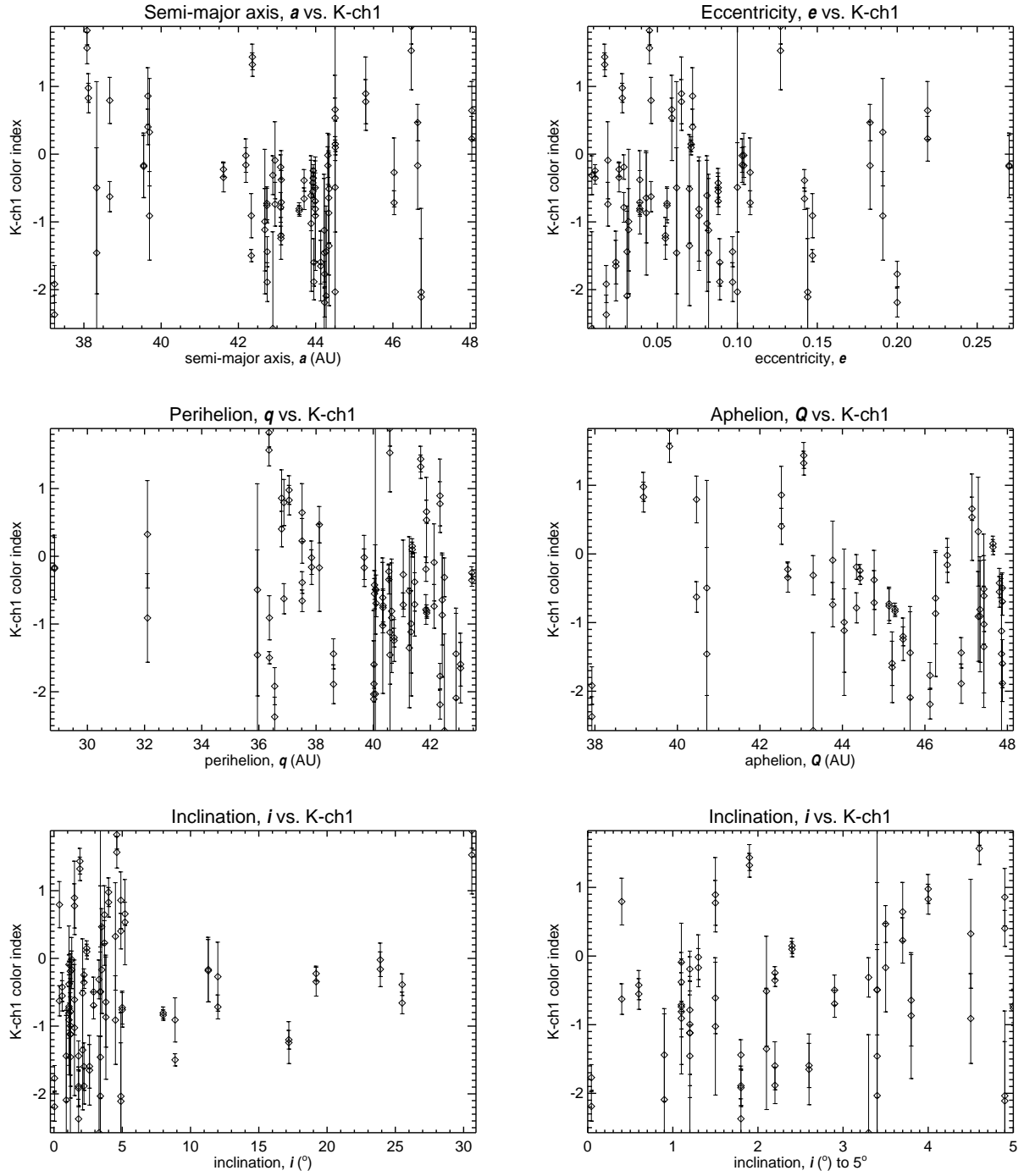


Figure 4.6: Plots of K-ch1 color as a function of orbital parameters semi-major axis (a), eccentricity (e), perihelion (q), aphelion (Q) and inclination (i). a , q , and Q are in units of AU; i is in units of degrees. The lower right plot is a zoomed in view of orbital inclination of the objects from 0 to 5°.

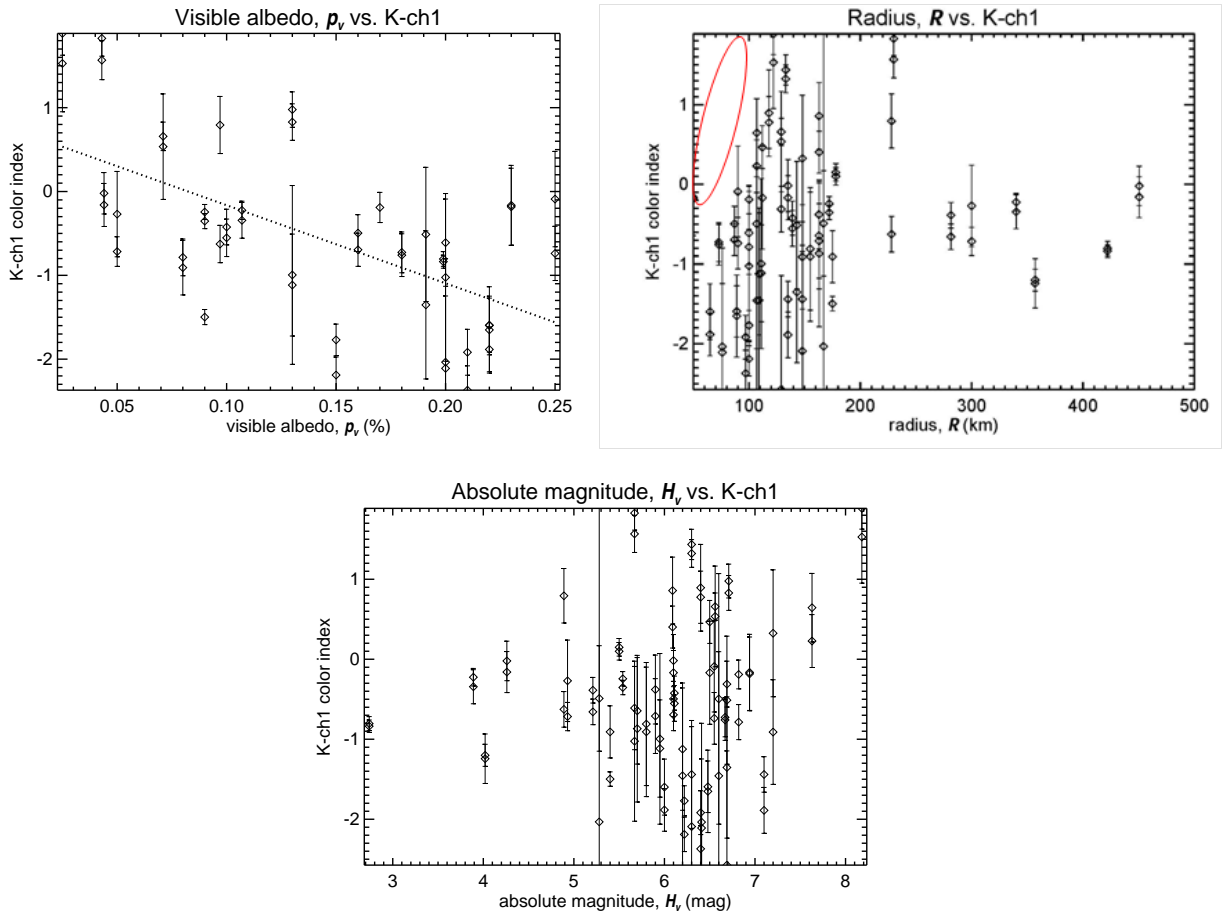


Figure 4.7: Physical characteristics vs. K-ch1 color. Icier bodies have higher albedos and deeper absorptions leading to an anti-correlation (black dotted line, $R^2 = 0.36$). The lack of small objects with positive K-ch1 color (red oval) is an observational bias.

Some structure in the plots of physical characteristics and K-ch1 color can be seen (fig. 4.7). A slight correlation is present in K-ch1 versus p_v , black line on the upper left plot. This is reasonable because higher albedo bodies are icier and therefore have deeper absorptions. The lack of small bodies with positive K-ch1 colors (red oval) is an observational bias. Icy bodies that have higher albedo and deeper absorptions (more negative K-ch1) are more detectable than non-icy, dark bodies. As detection and observation techniques become more sensitive, the area encircled should fill as more small dark objects are found. No correlation is noticed between absolute magnitude and K-ch1 color.

5. Discussion

The six objects with enough data (K-band, IRAC ch1 and ch2) for surface composition analysis are surprisingly diverse in composition. Varuna shows indication of organics on its surface. With a higher inclination and orbit more properly classified as a hot classical object, Varuna may have undergone more thermal processing than most of the other objects in this sample. The surface of Quaoar is found to be water ice, agreeing with previously published analyses (Jewitt and Luu, 2004; Dalle Ore et al., 2009). Ices are detected, for the first time, on Chaos, 2002 KX14, 2000 OK67, and Borasisi. 2002 KX14 and Chaos have colors that do not fit any end member composition and are of mixed surface composition. 2002 KX14 has a large water ice fraction as it is photometrically similar to an object that has surface water ice. The red V-K slopes of these objects are the result of red organic material embedded in the ices on their surfaces.

For the first time, methane is detected on the surface of Borasisi. The presence of methane on Borasisi is surprising, as methane is not expected to be retained over the age of the Solar System on the surface of a body as small as Borasisi, $R = 66\text{-}139$ km (Schaller and Brown, 2007b). Several scenarios for the retention of methane are possible. First, atmospheric escape may not be as efficient on cold classical bodies as expected. Second, an organic irradiation crust may have formed on the surface of Borasisi, trapping and preventing the escape of methane. Third, resurfacing of Borasisi may have exposed subsurface methane. It seems likely that if ion irradiation is vigorous enough to form organics, atmospheric escape would be efficient enough for the loss methane. Borasisi also has a red V-K color, indicating organic material on the surface. Reddening caused by simple organic grains embedded in methane ice (Brunetto et al., 2006) is likely what we are seeing in the photometry of Borasisi.

Methanol has been observed on Pholus, 55638 2002 VE95, and 26181 1996 GQ21 (Barucci et al., 2006; Cruikshank et al., 1998; Barucci et al., 2008). Methanol is less volatile than methane and some may be expected to remain on a small body like 2000 OK67. However, methanol is expected to be irradiated into more complex molecules (Brunetto et al., 2006). The presence of methanol on 2000 OK67 points to a primordial surface or some resurfacing mechanism, such as collisions.

The majority (78%) of the 46 cold classical objects in our sample have some indication of absorptions from ices or organics. Among the objects with published vis-NIR data and secure IRAC observations, eight of eleven (73%) show unambiguous absorption in IRAC ch1 and all of them have some indication of absorption. It is important to note that none of the seven objects that have positive K-ch1 have published K-band data and are assessed using sample averaged data. The high fraction of cold classical objects with absorptions supports my hypothesis that these objects retain their volatile materials, with some caveats. Correlation of the depth of absorption and the redness of the spectral slope, V- to K-band, suggests absorptions could be from organic materials on the surfaces of these objects. These organic materials are products of volatile ices irradiated by solar winds and chemically altered to more complex organic molecules (Brunetto et al., 2006). An organic signature is an indication that the ices have been retained on the surface and chemically altered rather than lost during thermal evolution.

Two inflection points can be seen in the slope of K-ch1 versus object in fig. 4.2. It is instructive to compare the spectral groups suggested by Barucci et al. (2008) with these slopes. The upper, steep slope is difficult to assess because the K-band data for those objects is sample averaged. The objects in the middle show a moderate slope and moderate absorptions caused by featureless (at these wavelengths) silicates mixed in with ices. Borasisi, shown here to be methane rich, is at the higher end of the slope and falls into the first spectral group. Chaos is an intermediate object between the methane and water ice dominated objects. 2002 KX14 and Quaoar are water ice dominated and fall into the second spectral group. Varunas surface is a mixture of organics and ices. Water ice has been detected on Varuna. Organics are photolytic products of ices and intermediate simple hydrocarbons are likely still present. Varuna may be intermediate between the second and third spectral

Table 5.1: Spectral class in order of K-ch1 index.

Number	Name/designation	Spectral class	K-ch1		
66652	Borasisi	1	-0.49	+/-	0.15
19521	Chaos	1-2	-0.49	+/-	0.27
119951	2002 KX14	2	-0.63	+/-	0.22
50000	Quaoar	2	-0.82	+/-	0.06
20000	Varuna	2-3	-1.22	+/-	0.17
168537	2000 OK67	3	-2.07	+/-	0.75

groups. 2000 OK67, which is methanol or hydrocarbon rich, is at the extreme left or deepest absorption end of fig. 4.2. Moving right to left on the figure, or moderate to deep absorption, the objects transition from one spectral class to the next nicely (table 5.1). The transitional objects Chaos and Varuna suggest there may be a continuum of spectral shapes rather than discrete groups.

By using sample averaged colors for objects without published NIR photometric data, the assumption is cold classical objects that have similar visible slopes have similar NIR spectral shapes. Because of the similar red color among the cold classical objects, this seems reasonable, but may prove to be incorrect. Vis-NIR *HST* photometric data provides a visual means to assess how well the sample averaged colors fit the spectral shape of an object. Four objects, 2003 GH55, 2001 QS322, 2001 QX297, and 88611 Teharonhiawako, have sample averaged K-band data that are higher in albedo than the *HST* data. A possible explanation for this is that our average is higher than the absorptions from the materials actually present on these specific bodies. However, for four other objects, 2001 RZ143, 2001 KK76, 2006 HW122, and 2003 QA92, the shape of the *HST* data agrees with the sample averaged albedos. The *HST* narrow band data is sensitive to narrower absorptions than would be seen with broadband NIR standard filters and these absorptions may not strongly affect the overall shape of the spectrum of an object. Future NIR photometry of cold classical objects will help better combine these data sets and refine the average NIR colors for cold classical objects.

Omitting objects classified as cold classical by the Petit et al. (2011) scheme, but not by the Gladman et al. (2008) scheme and resonant objects, does not significantly affect the analysis. If these objects are omitted, all of the remaining objects with K-band data and a secure ch1 observation still show an indication of an absorption. The percentage of objects

with absorptions for sample averaged K-band data do not significantly change. Only 58% of the upper limits indicate clear absorptions, a decrease of 11%. However, upper limits cannot confirm the absence of an absorption.

No correlation of colors and orbital parameters was found. Any signature of a chemical gradient across the cold classical population is not seen in these data. The narrow span that the cold classicals occupy may be too narrow to exhibit any gradient. The lack of obvious correlation between IR absorptions and orbital parameters supports the hypothesis that thermal processes have not affected the cold classical belt in any systematic way. Physical characteristics display weak correlations with color, but these are likely because of observational biases.

The presence of ices and organics on the surfaces of cold classical objects indicates these objects formed far from the Sun as required by many Solar System formation models. These materials also suggest the cold classicals have remained dynamically stable throughout the lifetime of the Solar System.

These *Spitzer* observations of cold classical KBOs are part of a larger program that includes 170 additional objects, two detached, 29 hot classical, 39 resonant, 40 scattered, 43 Centaurs, and 17 Trojan asteroids. With these other IRAC data, similar composition studies of other Kuiper Belt classes and Centaurs can be done. Many objects lack supporting ground based data and observations are in progress. Comparison of the dynamical classes will be interesting to assess whether these results are unique to the cold classical population.

James Webb Space Telescope (JWST) will provide exciting capabilities to further assess the composition of Kuiper Belt Objects. The Near Infrared Camera (NIRCam) and Near Infrared Spectrograph (NIRSpec) will have a spectral range of 0.6-5 μm and sensitivity as low as ~ 11 nJy in the wide band photometric filters. More sensitive spectra and photometric observations of KBOs will bolster and constrain our understanding of the nature of their surfaces. Technical details of the *JWST* suite of instruments can be found on the science website¹.

A required objective of the New Horizons mission, expected to arrive at the Pluto system in 2015, is to collect visible and infrared spectra and thus compositionally map the surfaces

¹<http://www.stsci.edu/jwst/>

of Pluto and Charon. The MVIC (Multi-spectral Visible Imaging Camera) is a panchromatic mapping camera that also images three broad-band colors, blue (0.40-0.55 μm), red (0.54-0.70 μm) and near-IR (0.780-0.975 μm), as well as a narrow band filter at 0.860-0.910 μm that will map the strong CH_4 feature at 0.89 μm . LEISA (Linear Etalon Imaging Spectral Array) is a 1.25-2.5 μm spectrometer designed to map absorption features of species previously discovered on Pluto (Young et al., 2008). Detailed understanding of one of the largest KBOs will test current and guide future hypotheses about KBO formation and evolution.

Conclusions

We find that most of the cold classical objects have absorptions in IRAC ch1. These absorptions are from ices of H_2O and CH_4 or organic materials derived from these ices. For six objects with secure observation in ch2, we assess gross surface composition. The surface of 20000 Varuna is composed largely of organic material, possible remnants of irradiated ices. 50000 Quaoar is found to have a surface of mostly water ice, agreeing with previously published findings. For the first time, ices are observed on four objects: 19521 Chaos, 119951 2002 KX14, 66652 Borasisi, and 138537 2000 OK67. Chaos has a mixture of surface ices and organics. 2002 KX14 is likely a mixture of materials with a large fraction of water ice.

Borasisi and 2000 OK67 are particularly intriguing. Borasisi has a surface composed largely of methane. This is surprising because methane is thought to escape from bodies as small as Borasisi over the age of the Solar System. Methanol and light hydrocarbons are found on the surface of 2000 OK67. Over the age of the Solar System methanol should have been irradiated into organics. Both discoveries require the surface of these bodies to be primordial or resurfaced to explain the presence of these materials.

The presence of ices and organics agrees with the idea that the cold classical objects formed far from the Sun and have not been dynamically perturbed. The cold classicals have diverse compositions that exhibit a continuum of spectral shapes rather than discrete groups. Cold classical Kuiper Belt Objects are found to be rich in volatile ices and the organic materials. These findings are small steps toward a larger understanding. The study of these primitive objects in the far reaches of our corner of space provides a window into the history and formation of our Solar System.

The study herein is based on observations made with the *Spitzer Space Telescope*, which is operated by the Jet Propulsion Laboratory, California Institute of Technology under a contract with NASA. Support for this work was provided by NASA through an award issued by JPL/Caltech.

References

References

- Allen, R. L., Gladman, B., Kavelaars, J. J., Petit, J.-M., Parker, J. W., and Nicholson, P. (2006). Discovery of a Low-Eccentricity, High-Inclination Kuiper Belt Object at 58 AU. *ApJ*, 640:L83–L86. 3
- Barkume, K. M., Brown, M. E., and Schaller, E. L. (2008). Near-Infrared Spectra of Centaurs and Kuiper Belt Objects. *AJ*, 135:55–67. 27, 28, 29
- Barucci, M. A., Alvarez-Candal, A., Merlin, F., Belskaya, I. N., de Bergh, C., Perna, D., DeMeo, F., and Fornasier, S. (2011). New insights on ices in Centaur and Transneptunian populations. *Icarus*, 214:297–307. 6
- Barucci, M. A., Belskaya, I. N., Fulchignoni, M., and Birlan, M. (2005). Taxonomy of Centaurs and Trans-Neptunian Objects. *AJ*, 130:1291–1298. 28, 29
- Barucci, M. A., Brown, M. E., Emery, J. P., and Merlin, F. (2008). *Composition and Surface Properties of Transneptunian Objects and Centaurs*, pages 143–160. 1, 23, 35
- Barucci, M. A., Merlin, F., Dotto, E., Doressoundiram, A., and de Bergh, C. (2006). TNO surface ices. Observations of the TNO 55638 (2002 VE₉₅). *A&A*, 455:725–730. 23, 35
- Batygin, K., Brown, M. E., and Fraser, W. C. (2011). Retention of a Primordial Cold Classical Kuiper Belt in an Instability-Driven Model of Solar System Formation. *ApJ*, 738:13. 31
- Benecci, S. D., Noll, K. S., Grundy, W. M., Buie, M. W., Stephens, D. C., and Levison, H. F. (2009). The correlated colors of transneptunian binaries. *Icarus*, 200:292–303. x, 19, 59, 71

- Benecchi, S. D., Noll, K. S., Stephens, D. C., Grundy, W. M., and Rawlins, J. (2011). Optical and infrared colors of transneptunian objects observed with HST. *Icarus*, 213:693–709. x, 19, 59, 70, 71
- Brown, M. E. (2008). *The Largest Kuiper Belt Objects*, pages 335–344. 23
- Brown, M. E., Barkume, K. M., Ragozzine, D., and Schaller, E. L. (2007). A collisional family of icy objects in the Kuiper belt. *Nature*, 446:294–296. 23
- Brown, M. E., Schaller, E. L., and Fraser, W. C. (2011). A Hypothesis for the Color Diversity of the Kuiper Belt. *ApJ*, 739:L60. 23, 31
- Brown, M. E., Trujillo, C., and Rabinowitz, D. (2004). Discovery of a Candidate Inner Oort Cloud Planetoid. *ApJ*, 617:645–649. 3
- Brown, M. E., Trujillo, C. A., and Rabinowitz, D. L. (2005). Discovery of a Planetary-sized Object in the Scattered Kuiper Belt. *ApJ*, 635:L97–L100. 3
- Brown, R. H., Cruikshank, D. P., and Pendleton, Y. (1999). Water Ice on Kuiper Belt Object 1996 TO₆₆. *ApJ*, 519:L101–L104. 23
- Brown, R. H., Cruikshank, D. P., Pendleton, Y. J., and Veeder, G. J. (1997). Surface composition of Kuiper Belt object 1993 SC. *Science*, 276:937–939. 23
- Brucker, M. J., Grundy, W. M., Stansberry, J. A., Spencer, J. R., Sheppard, S. S., Chiang, E. I., and Buie, M. W. (2009). High albedos of low inclination Classical Kuiper belt objects. *Icarus*, 201:284–294. 59
- Brunetto, R., Barucci, M. A., Dotto, E., and Strazzulla, G. (2006). Ion Irradiation of Frozen Methanol, Methane, and Benzene: Linking to the Colors of Centaurs and Trans-Neptunian Objects. *ApJ*, 644:646–650. 34, 35
- Cameron, A. G. W. (1962). The formation of the sun and planets. *Icarus*, 1:13–69. 2
- Cruikshank, D. P., Roush, T. L., Bartholomew, M. J., Geballe, T. R., Pendleton, Y. J., White, S. M., Bell, J. F., Davies, J. K., Owen, T. C., de Bergh, C., Tholen, D. J., Bernstein,

- M. P., Brown, R. H., Tryka, K. A., and Dalle Ore, C. M. (1998). The Composition of Centaur 5145 Pholus. *Icarus*, 135:389–407. 23, 35
- Cruikshank, D. P. and Silvaggio, P. M. (1979). Triton - A satellite with an atmosphere. *ApJ*, 233:1016–1020. 23
- Dalle Ore, C. M., Barucci, M. A., Emery, J. P., Cruikshank, D. P., Dalle Ore, L. V., Merlin, F., Alvarez-Candal, A., de Bergh, C., Trilling, D. E., Perna, D., Fornasier, S., Mastrapa, R. M. E., and Dotto, E. (2009). Composition of KBO (50000) Quaoar. *A&A*, 501:349–357. 28, 34
- Dalle Ore, C. M., Fulchignoni, M., Cruikshank, D. P., Barucci, M. A., Brunetto, R., Campins, H., de Bergh, C., Debes, J. H., Dotto, E., Emery, J. P., Grundy, W. M., Jones, A. P., Mennella, V., Orthous-Daunay, F. R., Owen, T., Pascucci, I., Pendleton, Y. J., Pinilla-Alonso, N., Quirico, E., and Strazzulla, G. (2011). Organic materials in planetary and protoplanetary systems: nature or nurture? *A&A*, 533:A98. 31
- Delsanti, A., Hainaut, O., Jourdeuil, E., Meech, K. J., Boehnhardt, H., and Barrera, L. (2004). Simultaneous visible-near IR photometric study of Kuiper Belt Object surfaces with the ESO/Very Large Telescopes. *A&A*, 417:1145–1158. 17, 59
- Delsanti, A. C., Boehnhardt, H., Barrera, L., Meech, K. J., Sekiguchi, T., and Hainaut, O. R. (2001). BVRI Photometry of 27 Kuiper Belt Objects with ESO/Very Large Telescope. *A&A*, 380:347–358. 59
- DeMeo, F. E., Fornasier, S., Barucci, M. A., Perna, D., Protopapa, S., Alvarez-Candal, A., Delsanti, A., Doressoundiram, A., Merlin, F., and de Bergh, C. (2009). Visible and near-infrared colors of Transneptunian objects and Centaurs from the second ESO large program. *A&A*, 493:283–290. 16, 59, 69
- Doressoundiram, A., Peixinho, N., de Bergh, C., Fornasier, S., Thébaud, P., Barucci, M. A., and Veillet, C. (2002). The Color Distribution in the Edgeworth-Kuiper Belt. *AJ*, 124:2279–2296. 17

- Doressoundiram, A., Peixinho, N., Doucet, C., Mousis, O., Barucci, M. A., Petit, J. M., and Veillet, C. (2005). The Meudon Multicolor Survey (2MS) of Centaurs and trans-neptunian objects: extended dataset and status on the correlations reported. *Icarus*, 174:90–104. 57, 59
- Doressoundiram, A., Peixinho, N., Moullet, A., Fornasier, S., Barucci, M. A., Beuzit, J.-L., and Veillet, C. (2007). The Meudon Multicolor Survey (2MS) of Centaurs and Trans-Neptunian Objects: From Visible to Infrared Colors. *AJ*, 134:2186–2199. 59
- Edgeworth, K. E. (1943). The evolution of our planetary system. *Journal of the British Astronomical Association*, 53:181–188. 2
- Elliot, J. L., Kern, S. D., Clancy, K. B., Gulbis, A. A. S., Millis, R. L., Buie, M. W., Wasserman, L. H., Chiang, E. I., Jordan, A. B., Trilling, D. E., and Meech, K. J. (2005). The Deep Ecliptic Survey: A Search for Kuiper Belt Objects and Centaurs. II. Dynamical Classification, the Kuiper Belt Plane, and the Core Population. *AJ*, 129:1117–1162. 3
- Emery, J. P., Dalle Ore, C. M., Cruikshank, D. P., Fernández, Y. R., Trilling, D. E., and Stansberry, J. A. (2007). Ices on (90377) Sedna: confirmation and compositional constraints. *A&A*, 466:395–398. 9, 12
- Fazio, G. G., Hora, J. L., Allen, L. E., Ashby, M. L. N., Barmby, P., Deutsch, L. K., Huang, J.-S., Kleiner, S., Marengo, M., Megeath, S. T., Melnick, G. J., Pahre, M. A., Patten, B. M., Polizotti, J., Smith, H. A., Taylor, R. S., Wang, Z., Willner, S. P., Hoffmann, W. F., Pipher, J. L., Forrest, W. J., McMurty, C. W., McCreight, C. R., McKelvey, M. E., McMurray, R. E., Koch, D. G., Moseley, S. H., Arendt, R. G., Mentzell, J. E., Marx, C. T., Losch, P., Mayman, P., Eichhorn, W., Krebs, D., Jhabvala, M., Gezari, D. Y., Fixsen, D. J., Flores, J., Shakoorzadeh, K., Jungo, R., Hakun, C., Workman, L., Karpati, G., Kichak, R., Whitley, R., Mann, S., Tollestrup, E. V., Eisenhardt, P., Stern, D., Gorjian, V., Bhattacharya, B., Carey, S., Nelson, B. O., Glaccum, W. J., Lacy, M., Lowrance, P. J., Laine, S., Reach, W. T., Stauffer, J. A., Surace, J. A., Wilson, G., Wright, E. L., Hoffman, A., Domingo, G., and Cohen, M. (2004). The Infrared Array Camera (IRAC) for the Spitzer Space Telescope. *ApJS*, 154:10–17. 9

- Fernandez, J. A. (1980). On the existence of a comet belt beyond Neptune. *MNRAS*, 192:481–491. 2
- Fraser, W. C. and Brown, M. E. (2012). The Hubble Wide Field Camera 3 Test of Surfaces in the Outer Solar System: The Compositional Classes of the Kuiper Belt. *ApJ*, 749:33. x, 19, 59, 72, 73
- Fulchignoni, M., Belskaya, I., Barucci, M. A., de Sanctis, M. C., and Doressoundiram, A. (2008). *Transneptunian Object Taxonomy*, pages 181–192. 29, 59
- Giorgini, J. D., Yeomans, D. K., Chamberlin, A. B., Chodas, P. W., Jacobson, R. A., Keesey, M. S., Lieske, J. H., Ostro, S. J., Standish, E. M., and Wimberly, R. N. (1996). JPL’s On-Line Solar System Data Service. In *AAS/Division for Planetary Sciences Meeting Abstracts #28*, volume 28 of *Bulletin of the American Astronomical Society*, page 1158. 12
- Gladman, B., Marsden, B. G., and Vanlaerhoven, C. (2008). *Nomenclature in the Outer Solar System*, pages 43–57. 3, 4, 5, 15, 36
- Grundy, W. M., Noll, K. S., Buie, M. W., Benecchi, S. D., Stephens, D. C., and Levison, H. F. (2009). Mutual orbits and masses of six transneptunian binaries. *Icarus*, 200:627–635. 59
- Guilbert, A., Alvarez-Candal, A., Merlin, F., Barucci, M. A., Dumas, C., de Bergh, C., and Delsanti, A. (2009). ESO-Large Program on TNOs: Near-infrared spectroscopy with SINFONI. *Icarus*, 201:272–283. 28
- Hapke, B. (1993). *Theory of reflectance and emittance spectroscopy*. 23
- Jewitt, D. and Luu, J. (1993). Discovery of the candidate Kuiper belt object 1992 QB1. *Nature*, 362:730–732. 2
- Jewitt, D. C. and Luu, J. (2004). Crystalline water ice on the Kuiper belt object (50000) Quaoar. *Nature*, 432:731–733. 8, 28, 34

- Jewitt, D. C. and Luu, J. X. (2001). Colors and Spectra of Kuiper Belt Objects. *AJ*, 122:2099–2114. 22
- Kavelaars, J., Jones, L., Gladman, B., Parker, J. W., and Petit, J.-M. (2008). *The Orbital and Spatial Distribution of the Kuiper Belt*, pages 59–69. 15
- Kowal, C. T. and Gehrels, T. (1977). Slow-Moving Object Kowal. *IAU Circ.*, 3129:1. 2
- Kuiper, G. P. (1951). On the Origin of the Solar System. In Hynek, J. A., editor, *50th Anniversary of the Yerkes Observatory and Half a Century of Progress in Astrophysics*, page 357. 2
- Leonard, F. C. (1930). The New Planet Pluto. *Leaflet of the Astronomical Society of the Pacific*, 1:121. 2
- Levison, H. F., Morbidelli, A., Van Laerhoven, C., Gomes, R., and Tsiganis, K. (2008). Origin of the structure of the Kuiper belt during a dynamical instability in the orbits of Uranus and Neptune. *Icarus*, 196:258–273. 1, 4, 31
- Licandro, J., Oliva, E., and Di Martino, M. (2001). NICS-TNG infrared spectroscopy of trans-neptunian objects 2000 EB173 and 2000 WR106. *A&A*, 373:L29–L32. 28
- Luu, J., Jewitt, D., and Marsden, B. G. (1993). 1993 FW. *IAU Circ.*, 5730:1. 2
- Luu, J., Marsden, B., Jewitt, D., Trujillo, C., and Chen, J. (1997). A New Dynamical Class in the Outer Solar System. In *AAS/Division for Planetary Sciences Meeting Abstracts #29*, volume 29 of *Bulletin of the American Astronomical Society*, page 1020. 3
- Luu, J. X. and Jewitt, D. C. (1998). Optical and Infrared Reflectance Spectrum of Kuiper Belt Object 1996 TL 66. *ApJ*, 494:L117. 23
- Lykawka, P. S. and Mukai, T. (2007). Dynamical classification of trans-neptunian objects: Probing their origin, evolution, and interrelation. *Icarus*, 189:213–232. 1
- McBride, N., Green, S. F., Davies, J. K., Tholen, D. J., Sheppard, S. S., Whiteley, R. J., and Hillier, J. K. (2003). Visible and infrared photometry of Kuiper Belt objects: searching for evidence of trends. *Icarus*, 161:501–510. 59

- Müller, T. G., Lellouch, E., Stansberry, J., Kiss, C., Santos-Sanz, P., Vilenius, E., Protopapa, S., Moreno, R., Mueller, M., Delsanti, A., Duffard, R., Fornasier, S., Groussin, O., Harris, A. W., Henry, F., Horner, J., Lacerda, P., Lim, T., Mommert, M., Ortiz, J. L., Rengel, M., Thirouin, A., Trilling, D., Barucci, A., Crovisier, J., Doressoundiram, A., Dotto, E., Gutiérrez, P. J., Hainaut, O. R., Hartogh, P., Hestroffer, D., Kidger, M., Lara, L., Swinyard, B., and Thomas, N. (2010). “TNOs are Cool”: A survey of the trans-Neptunian region. I. Results from the Herschel science demonstration phase (SDP). *A&A*, 518:L146. 59
- Noll, K. S., Grundy, W. M., Schlichting, H. E., Murray-Clay, R. A., and Benecchi, S. D. (2012). Resonant Transneptunian Binaries: Evidence for Slow Migration of Neptune. In *AAS/Division for Planetary Sciences Meeting Abstracts*, volume 44 of *AAS/Division for Planetary Sciences Meeting Abstracts*, page 405.07. 15
- Noll, K. S., Grundy, W. M., Stephens, D. C., Levison, H. F., and Kern, S. D. (2008). Evidence for two populations of classical transneptunian objects: The strong inclination dependence of classical binaries. *Icarus*, 194:758–768. 4
- Peixinho, N., Boehnhardt, H., Belskaya, I., Doressoundiram, A., Barucci, M. A., and Delsanti, A. (2004). ESO large program on Centaurs and TNOs: visible colors-final results. *Icarus*, 170:153–166. 60
- Petit, J.-M., Kavelaars, J. J., Gladman, B. J., Jones, R. L., Parker, J. W., Van Laerhoven, C., Nicholson, P., Mars, G., Rousselot, P., Mousis, O., Marsden, B., Bieryla, A., Taylor, M., Ashby, M. L. N., Benavidez, P., Campo Bagatin, A., and Bernabeu, G. (2011). The Canada-France Ecliptic Plane Survey Full Data Release: The Orbital Structure of the Kuiper Belt. *AJ*, 142:131. x, 15, 30, 36, 68
- Rabinowitz, D. L., Schaefer, B. E., and Tourtellotte, S. W. (2007). The Diverse Solar Phase Curves of Distant Icy Bodies. I. Photometric Observations of 18 Trans-Neptunian Objects, 7 Centaurs, and Nereid. *AJ*, 133:26–43. 14
- Reach, W. T., Megeath, S. T., Cohen, M., Hora, J., Carey, S., Surace, J., Willner, S. P., Barmby, P., Wilson, G., Glaccum, W., Lowrance, P., Marengo, M., and Fazio, G. G.

- (2005). Absolute Calibration of the Infrared Array Camera on the Spitzer Space Telescope. *PASP*, 117:978–990. 12
- Santos-Sanz, P., Ortiz, J. L., Barrera, L., and Boehnhardt, H. (2009). New BVRI photometry results on Kuiper Belt Objects from the ESO VLT. *A&A*, 494:693–706. 18, 19, 60
- Schaller, E. L. and Brown, M. E. (2007a). Detection of Methane on Kuiper Belt Object (50000) Quaoar. *ApJ*, 670:L49–L51. 28
- Schaller, E. L. and Brown, M. E. (2007b). Volatile Loss and Retention on Kuiper Belt Objects. *ApJ*, 659:L61–L64. 34
- Sheppard, S. S. (2012). The Ultra-Red Color of Kuiper Belt Objects in the 5:3 and 7:4 Mean Motion Neptune Resonances. In *AAS/Division for Planetary Sciences Meeting Abstracts*, volume 44 of *AAS/Division for Planetary Sciences Meeting Abstracts*, page 405.02. 15, 16, 30, 57, 60
- Sheppard, S. S., Lacerda, P., and Ortiz, J. L. (2008). *Photometric Lightcurves of Transneptunian Objects and Centaurs: Rotations, Shapes, and Densities*, pages 129–142. 20
- Smith, E. V. P. and Gottlieb, D. M. (1974). Solar flux and its variations. *Space Sci. Rev.*, 16:771–802. 12
- Stansberry, J., Grundy, W., Brown, M., Cruikshank, D., Spencer, J., Trilling, D., and Margot, J.-L. (2008). *Physical Properties of Kuiper Belt and Centaur Objects: Constraints from the Spitzer Space Telescope*, pages 161–179. 14, 57, 60
- Tegler, S. C. and Romanishin, W. (2000). Extremely red Kuiper-belt objects in near-circular orbits beyond 40 AU. *Nature*, 407:979–981. 4
- Tholen, D. J., Senay, M., Hainaut, O., and Marsden, B. G. (1994). 1993 RO, 1993 RP, 1993 SB, 1993 SC. *IAU Circ.*, 5983:1. 3
- Trujillo, C. and Marsden, B. G. (1999). 1999 CF119. *Minor Planet Electronic Circulars*, page 44. 3

- Trujillo, C., Sheppard, S., and Schaller, E. (2011). A Photometric System for Detection of Water and Methane Ices on Kuiper Belt Objects. In *EPSC-DPS Joint Meeting 2011*, page 545. viii, x, 16, 59, 60, 69
- Trujillo, C. A. and Brown, M. E. (2002). A Correlation between Inclination and Color in the Classical Kuiper Belt. *ApJ*, 566:L125–L128. 4
- Tsiganis, K., Gomes, R., Morbidelli, A., and Levison, H. F. (2005). Origin of the orbital architecture of the giant planets of the Solar System. *Nature*, 435:459–461. 1
- Vilas, F. and Gaffey, M. J. (1989). Phyllosilicate absorption features in main-belt and outer-belt asteroid reflectance spectra. *Science*, 246:790–792. 22
- Vilenius, E., Kiss, C., Mommert, M., Müller, T., Santos-Sanz, P., Pal, A., Stansberry, J., Mueller, M., Peixinho, N., Fornasier, S., Lellouch, E., Delsanti, A., Thirouin, A., Ortiz, J. L., Duffard, R., Perna, D., Szalai, N., Protopapa, S., Henry, F., Hestroffer, D., Rengel, M., Dotto, E., and Hartogh, P. (2012). "TNOs are Cool": A survey of the trans-Neptunian region. VI. Herschel/PACS observations and thermal modeling of 19 classical Kuiper belt objects. *A&A*, 541:A94. 60
- Whipple, F. L. (1964a). Evidence for a Comet Belt beyond Neptune. *Proceedings of the National Academy of Science*, 51:711–718. 2
- Whipple, F. L. (1964b). The History of the Solar System. *Proceedings of the National Academy of Science*, 52:565–594. 2
- Young, L. A., Stern, S. A., Weaver, H. A., Bagenal, F., Binzel, R. P., Buratti, B., Cheng, A. F., Cruikshank, D., Gladstone, G. R., Grundy, W. M., Hinson, D. P., Horanyi, M., Jennings, D. E., Linscott, I. R., McComas, D. J., McKinnon, W. B., McNutt, R., Moore, J. M., Murchie, S., Olkin, C. B., Porco, C. C., Reitsema, H., Reuter, D. C., Spencer, J. R., Slater, D. C., Strobel, D., Summers, M. E., and Tyler, G. L. (2008). New Horizons: Anticipated Scientific Investigations at the Pluto System. *Space Sci. Rev.*, 140:93–127. 38

Appendix

A. IRAC observational data

Data from IRAC observations are presented here. Albedo is calculated from flux as described in the text.

Table A.1: IRAC fluxes and converted albedos.

Name (desination)	Date	Fluxes (μJy)		Albedos		pv	R(km)	pv & R Source
		ch1	ch2	ch1	ch2			
50000 Quaoar	15-Sep-05	28.00 \pm 1.28	14.06 \pm 1.26	0.263 \pm 0.012	0.201 \pm 0.018	0.199	422	Sta08
	18-Sep-05	28.78 \pm 1.74	16.46 \pm 1.75	0.271 \pm 0.016	0.236 \pm 0.025			
20000 Varuna	24-Mar-06	9.48 \pm 2.52	9.24 \pm 1.59	0.075 \pm 0.020	0.112 \pm 0.019	0.088	357	Bru09
	29-Mar-06	9.76 \pm 0.77	6.33 \pm 1.18	0.078 \pm 0.006	0.077 \pm 0.023			
66652 Borasisi	26-Dec-07	2.38 \pm 0.45	2.97 \pm 0.63	0.175 \pm 0.033	0.332 \pm 0.071	0.1	139	Bru09
	31-Dec-07	2.67 \pm 0.47	4.07 \pm 1.01	0.197 \pm 0.035	0.458 \pm 0.114			
19521 Chaos	19-Oct-07	5.26 \pm 0.64	5.02 \pm 0.81	0.055 \pm 0.007	0.080 \pm 0.013	0.05	300	Vil12
	23-Oct-07	7.99 \pm 3.63	5.08 \pm 2.05	0.083 \pm 0.038	0.080 \pm 0.032			
79360 1997 CS29	7-May-08	0.59 \pm 0.16	0.60 \pm 0.12	0.042 \pm 0.012	0.255*	0.09	172	Vil12
	9-May-08	0.53 \pm 0.15	0.67 \pm 0.08	0.038 \pm 0.011	0.183*			

Continued on next page

Table A.1: continued

Name (desination)	Date	Fluxes (μJy)		Albedos		pv	R(km)	Source
		ch1	ch2	ch1	ch2			
119951 2002 KX14	16-Sep-08	26.84+/-6.65	4.23+/-1.02	0.614+/-0.156*	0.147+/-0.036	0.097	228	Sta08
	20-Sep-08	7.22+/-0.51	4.56+/-0.78	0.166+/-0.015	0.160+/-0.029			
134860 2000 OJ67	22-Nov-07	1.53+/-0.39	0.88+/-0.43*	0.290+/-0.075	0.254+/-0.125*	0.1 1	90	Bru09
	25-Nov-07	2.75+/-1.39	2.90+/-1.56*	0.527+/-0.265	0.844+/-0.455*			
35671 1998 SN165	29-Jan-10	5.26+/-0.76	3.79+/-0.65	0.305+/-0.045	0.335+/-0.057	0.043	230	Sta08
	3-Feb-10	4.10+/-0.70	3.08+/-0.62	0.240+/-0.041	0.274+/-0.055			
138537 2000 OK67	13-Jan-10	0.86+/-0.68	1.96+/-0.61	0.113+/-0.089	0.392+/-0.122	0.2	76	Vil12
	17-Jan-10	0.92+/-1.04	3.34+/-0.98	0.121+/-0.137	0.670+/-0.198			
2002 GV31	25-Jun-10	3.22+/-0.73	1.01+/-0.62	0.103+/-0.023	0.050+/-0.030	0.22 1	65	Vil12
	29-Jun-10	4.14+/-1.26	1.46+/-0.54	0.134+/-0.041	0.072+/-0.027			
2003 GH55	24-Mar-10	2.06+/-1.45		0.116+/-0.081		0.088a	155	Sta08
	28-Mar-10	1.90+/-1.39		0.106+/-0.078				
2005 EF298	15-Jun-10	1.60+/-0.28		0.269+/-0.047*		0.16	87	Vil12
	19-Jun-10	1.32+/-0.25		0.224+/-0.034*				
Teharonhiawako	2-Jan-10	2.16+/-0.98		0.130+/-0.059		0.22	89	Vil12
	6-Jan-10	2.28+/-0.60		0.137+/-0.036				
303712 2005 PR21	12-Jan-10	3.05+/-0.86		0.230+/-0.065		0.088a	135	Sta08
	16-Jan-10	2.64+/-0.61		0.200+/-0.047				

Continued on next page

Table A.1: continued

Name (desination)	Date	Fluxes (μJy)		Albedos		pv	R(km)	pv & R Source
		ch1	ch2	ch1	ch2			
2003 WU188	18-Nov-09	1.66+/-1.39		0.105+/-0.088		0.088a	163	Sta08
	22-Nov-09	2.05+/-1.24		0.129+/-0.078				
2001 QO297	23-Jan-10	2.27+/-0.83		0.171+/-0.063		0.088a	163	Sta08
	27-Jan-10	1.66+/-0.67		0.126+/-0.051				
168703 2000 GP183	4-Sep-09	3.44+/-0.68		0.232+/-0.046		0.088a	163	Dor05b
	7-Sep-09	5.22+/-1.87		0.353+/-0.127				
135182 2001 QT322	23-Jan-10	0.63+/-0.14		0.060+/-0.013		0.21 1	97	Bru09
	28-Jan-10	2.54+/-2.05		0.091+/-0.018				
2000 CN105	26-Jun-10	0.36+/-1.45	1.43+/-0.56	0.028+/-0.113	0.169+/-0.066	0.088a	167	Pei04
	1-Jul-10	1.48+/-0.78	1.48+/-0.53	0.116+/-0.061	0.177+/-0.063			
2002 VT130	30-Oct-09	1.35+/-0.73		0.119+/-0.064		0.13 1	111	Br09(mod)
	3-Nov-09	1.51+/-1.47		0.133+/-0.129				
2001 RZ143	5-Sep-09	1.69+/-1.34		0.118+/-0.094		0.191	143	Vil12
	10-Sep-09	3.67+/-2.63		0.256+/-0.184				
2003 QA92	2-Jan-10	2.03+/-2.91		0.148+/-0.213		0.088a	107	Sta08
	6-Jan-10	0.84+/-1.19		0.061+/-0.087				
2001 QX297	11-Jan-10	0.80+/-0.49		0.062+/-0.038		0.088	148	Sta08
	15-Jan-10	0.43+/-0.50		0.034+/-0.039				

Continued on next page

Table A.1: continued

Name (desination)	Date	Fluxes (μJy)		Albedos		pv	R(km)	pv & R Source																																																																																																												
		ch1	ch2	ch1	ch2																																																																																																															
2006 HW122	16-Sep-09	4.17+/-2.04		0.532+/-0.260		0.088	118	Sta08																																																																																																												
	20-Sep-09	3.72+/-1.05		0.477+/-0.135					88268 2001 KK76	23-Sep-09	11.85+/-1.25		0.976+/-0.103*		0.088a	133	Sta08	27-Sep-09	13.02+/-1.64		1.083+/-0.137*		1999 OJ4	6-Dec-09	1.56+/-0.21		0.720+/-0.098*		0.13u	47	Gr09	11-Dec-09	1.77+/-0.22		0.826+/-0.105*		2001 QD298	7-Dec-09	1.01+/-0.19		0.258+/-0.049*		0.18	73	Bru09	11-Dec-09	1.03+/-0.18		0.266+/-0.047*		2001 QS322	23-Jan-10	1.04+/-0.15	1.47+/-1.20	0.078+/-0.011*	0.168+/-0.137	0.15u	100	Bru09	28-Jan-10	0.71+/-0.12	1.97+/-1.45	0.053+/-0.009*	0.226+/-0.166	2004 VZ75	30-Oct-09	4.98+/-3.61*		0.315+/-0.228*		0.088a	148	Sta08	2-Nov-09	1.61+/-0.96*		0.101+/-0.060*		2001 QB298	11-Jan-10	0.63+/-0.15		0.041+/-0.010*		0.088a	135	Sta08	15-Jan-10	0.95+/-0.16		0.062+/-0.011*		60454 2000 CH105	5-Feb-10	0.62+/-0.66		0.067+/-0.071*		0.088a	109	Pei04	9-Feb-10	0.85+/-0.59		0.091+/-0.063*		1996 TK66	4-Sep-09	2.13+/-0.48		0.209+/-0.047		0.088	129	Sta08	8-Sep-09
88268 2001 KK76	23-Sep-09	11.85+/-1.25		0.976+/-0.103*		0.088a	133	Sta08																																																																																																												
	27-Sep-09	13.02+/-1.64		1.083+/-0.137*					1999 OJ4	6-Dec-09	1.56+/-0.21		0.720+/-0.098*		0.13u	47	Gr09	11-Dec-09	1.77+/-0.22		0.826+/-0.105*		2001 QD298	7-Dec-09	1.01+/-0.19		0.258+/-0.049*		0.18	73	Bru09	11-Dec-09	1.03+/-0.18		0.266+/-0.047*		2001 QS322	23-Jan-10	1.04+/-0.15	1.47+/-1.20	0.078+/-0.011*	0.168+/-0.137	0.15u	100	Bru09	28-Jan-10	0.71+/-0.12	1.97+/-1.45	0.053+/-0.009*	0.226+/-0.166	2004 VZ75	30-Oct-09	4.98+/-3.61*		0.315+/-0.228*		0.088a	148	Sta08	2-Nov-09	1.61+/-0.96*		0.101+/-0.060*		2001 QB298	11-Jan-10	0.63+/-0.15		0.041+/-0.010*		0.088a	135	Sta08	15-Jan-10	0.95+/-0.16		0.062+/-0.011*		60454 2000 CH105	5-Feb-10	0.62+/-0.66		0.067+/-0.071*		0.088a	109	Pei04	9-Feb-10	0.85+/-0.59		0.091+/-0.063*		1996 TK66	4-Sep-09	2.13+/-0.48		0.209+/-0.047		0.088	129	Sta08	8-Sep-09	0.26+/-0.34		0.026+/-0.034											
1999 OJ4	6-Dec-09	1.56+/-0.21		0.720+/-0.098*		0.13u	47	Gr09																																																																																																												
	11-Dec-09	1.77+/-0.22		0.826+/-0.105*					2001 QD298	7-Dec-09	1.01+/-0.19		0.258+/-0.049*		0.18	73	Bru09	11-Dec-09	1.03+/-0.18		0.266+/-0.047*		2001 QS322	23-Jan-10	1.04+/-0.15	1.47+/-1.20	0.078+/-0.011*	0.168+/-0.137	0.15u	100	Bru09	28-Jan-10	0.71+/-0.12	1.97+/-1.45	0.053+/-0.009*	0.226+/-0.166	2004 VZ75	30-Oct-09	4.98+/-3.61*		0.315+/-0.228*		0.088a	148	Sta08	2-Nov-09	1.61+/-0.96*		0.101+/-0.060*		2001 QB298	11-Jan-10	0.63+/-0.15		0.041+/-0.010*		0.088a	135	Sta08	15-Jan-10	0.95+/-0.16		0.062+/-0.011*		60454 2000 CH105	5-Feb-10	0.62+/-0.66		0.067+/-0.071*		0.088a	109	Pei04	9-Feb-10	0.85+/-0.59		0.091+/-0.063*		1996 TK66	4-Sep-09	2.13+/-0.48		0.209+/-0.047		0.088	129	Sta08	8-Sep-09	0.26+/-0.34		0.026+/-0.034																									
2001 QD298	7-Dec-09	1.01+/-0.19		0.258+/-0.049*		0.18	73	Bru09																																																																																																												
	11-Dec-09	1.03+/-0.18		0.266+/-0.047*					2001 QS322	23-Jan-10	1.04+/-0.15	1.47+/-1.20	0.078+/-0.011*	0.168+/-0.137	0.15u	100	Bru09	28-Jan-10	0.71+/-0.12	1.97+/-1.45	0.053+/-0.009*	0.226+/-0.166	2004 VZ75	30-Oct-09	4.98+/-3.61*		0.315+/-0.228*		0.088a	148	Sta08	2-Nov-09	1.61+/-0.96*		0.101+/-0.060*		2001 QB298	11-Jan-10	0.63+/-0.15		0.041+/-0.010*		0.088a	135	Sta08	15-Jan-10	0.95+/-0.16		0.062+/-0.011*		60454 2000 CH105	5-Feb-10	0.62+/-0.66		0.067+/-0.071*		0.088a	109	Pei04	9-Feb-10	0.85+/-0.59		0.091+/-0.063*		1996 TK66	4-Sep-09	2.13+/-0.48		0.209+/-0.047		0.088	129	Sta08	8-Sep-09	0.26+/-0.34		0.026+/-0.034																																							
2001 QS322	23-Jan-10	1.04+/-0.15	1.47+/-1.20	0.078+/-0.011*	0.168+/-0.137	0.15u	100	Bru09																																																																																																												
	28-Jan-10	0.71+/-0.12	1.97+/-1.45	0.053+/-0.009*	0.226+/-0.166				2004 VZ75	30-Oct-09	4.98+/-3.61*		0.315+/-0.228*		0.088a	148	Sta08	2-Nov-09	1.61+/-0.96*		0.101+/-0.060*		2001 QB298	11-Jan-10	0.63+/-0.15		0.041+/-0.010*		0.088a	135	Sta08	15-Jan-10	0.95+/-0.16		0.062+/-0.011*		60454 2000 CH105	5-Feb-10	0.62+/-0.66		0.067+/-0.071*		0.088a	109	Pei04	9-Feb-10	0.85+/-0.59		0.091+/-0.063*		1996 TK66	4-Sep-09	2.13+/-0.48		0.209+/-0.047		0.088	129	Sta08	8-Sep-09	0.26+/-0.34		0.026+/-0.034																																																					
2004 VZ75	30-Oct-09	4.98+/-3.61*		0.315+/-0.228*		0.088a	148	Sta08																																																																																																												
	2-Nov-09	1.61+/-0.96*		0.101+/-0.060*					2001 QB298	11-Jan-10	0.63+/-0.15		0.041+/-0.010*		0.088a	135	Sta08	15-Jan-10	0.95+/-0.16		0.062+/-0.011*		60454 2000 CH105	5-Feb-10	0.62+/-0.66		0.067+/-0.071*		0.088a	109	Pei04	9-Feb-10	0.85+/-0.59		0.091+/-0.063*		1996 TK66	4-Sep-09	2.13+/-0.48		0.209+/-0.047		0.088	129	Sta08	8-Sep-09	0.26+/-0.34		0.026+/-0.034																																																																			
2001 QB298	11-Jan-10	0.63+/-0.15		0.041+/-0.010*		0.088a	135	Sta08																																																																																																												
	15-Jan-10	0.95+/-0.16		0.062+/-0.011*					60454 2000 CH105	5-Feb-10	0.62+/-0.66		0.067+/-0.071*		0.088a	109	Pei04	9-Feb-10	0.85+/-0.59		0.091+/-0.063*		1996 TK66	4-Sep-09	2.13+/-0.48		0.209+/-0.047		0.088	129	Sta08	8-Sep-09	0.26+/-0.34		0.026+/-0.034																																																																																	
60454 2000 CH105	5-Feb-10	0.62+/-0.66		0.067+/-0.071*		0.088a	109	Pei04																																																																																																												
	9-Feb-10	0.85+/-0.59		0.091+/-0.063*					1996 TK66	4-Sep-09	2.13+/-0.48		0.209+/-0.047		0.088	129	Sta08	8-Sep-09	0.26+/-0.34		0.026+/-0.034																																																																																															
1996 TK66	4-Sep-09	2.13+/-0.48		0.209+/-0.047		0.088	129	Sta08																																																																																																												
	8-Sep-09	0.26+/-0.34		0.026+/-0.034																																																																																																																

Continued on next page

Table A.1: continued

Name (desination)	Date	Fluxes (μJy)		Albedos		pv	R(km)	pv & R Source
		ch1	ch2	ch1	ch2			
145452 2005 RN43	18-Dec-10	14.01+/-1.13	9.76+/-0.44*	0.154+/-0.013	0.164+/-0.008*	0.107	340	Vil12
	21-Dec-10	12.45+/-2.30	10.89+/-0.91*	0.138+/-0.026	0.184+/-0.015*			
1999 CD158	6-Jun-12	3.67+/-1.08*		0.136*		0.088a	281.4	Del01
	12-Jun-12	2.82+/-0.86*		0.106*				
120347 Salacia	23-Jan-10	9.34+/-1.64		0.083+/-0.015		0.044	450.5	Vil12
	26-Jan-10	8.20+/-1.58		0.073+/-0.014				
2007 TY430	30-Jan-10	2.46+/-0.84		0.350+/-0.124		0.23	50	She12
	3-Feb-10	2.39+/-0.78		0.344+/-0.116				
2000 QL251	29-Jan-10	2.97+/-1.07		0.298+/-0.108		0.088a	107	Sta08
	3-Feb-10	2.01+/-0.53		0.203+/-0.053				
148780 Altjira	10-Oct-09	2.35+/-1.31		0.292+/-0.163		0.07 1	129	Vil12
	14-Oct-09	-0.17+/-1.47		0.327*				
275809 2001 QY297	28-Nov-09	1.68+/-0.54		0.271+/-0.086		0.2	100	Vil12
	3-Dec-09	1.13+/-0.97		0.185+/-0.157				
2003 QR91	28-Nov-09	2.28+/-1.33		0.200+/-0.117		0.088a	112	Sta08
	3-Dec-09	4.03+/-0.91		0.359+/-0.081				
2001 QC298	25-Dec-09	2.77+/-1.32		0.156+/-0.074		0.025	122	Sta08
	28-Dec-09	0.14+/-1.08		0.217*				

Continued on next page

Table A.1: continued

Name (desination)	Date	Fluxes (μJy)		Albedos		pv	R(km)	pv & R Source
		ch1	ch2	ch1	ch2			
2003 QA91	9-Dec-09	3.13+/-1.25		0.256*		0.088a	178	Sta08
	13-Dec-09	2.95+/-1.61		0.268*				
2001 XR254	6-Dec-09					0.17	100	Vil12
	10-Dec-09	0.59+/-0.96		0.318*				
126154 2001 YH140	2-Jan-12	3.50+/-0.60		0.103+/-0.018		0.08	175	Mul10
	6-Jan-12	3.14+/-0.89		0.092+/-0.026				
48639 1995 TL8	3-Mar-11	1.48+/-0.34*		0.080*		0.09b	200	Dor05
	7-Mar-11	13.64+/-8.71*						

* - upper limit for flux or albedo reported.

^a - average KBO albedo from Stansberry et al. (2008).

^b - assumed p_v from Doressoundiram et al. (2005).

^l - lower limit for p_v .

^b - approximate p_v from Sheppard (2012).

B. Published photometric data

Published photometric data used in this analysis are presented here.

Table B.1: Published photometric data.

Name (desination)	B-V	V-R	V-I	Vis Ref	V-J	V-H	V-K	NIR Ref
48639 1995 TL8	1.04+/-0.07	0.69+/-0.05	1.33+/-0.09	Del04	2.42+/-0.05	2.82+/-0.09	2.80+/-0.09	Del04
1996 TK66	0.95+/-0.08	0.81+/-0.05	1.42+/-0.06	Dor02	2.16+/-0.13a		2.68+/-0.15a	–
79360 Sila-Nunam	1.08+/-0.03	0.66+/-0.04	1.25+/-0.03	Ful08&	2.06+/-0.03	2.44+/-0.08	2.48+/-0.09	Ful08&
35671 1998 SN165	0.82+/-0.08	0.33+/-0.08	0.84+/-0.08	Dor01&	1.27+/-0.05		1.73+/-0.14a	McB03
19521 Chaos	0.93+/-0.06	0.56+/-0.04	1.26+/-0.06	Del06	1.83+/-0.08	2.23+/-0.09	2.25+/-0.11	Del04&
1999 CD158	0.87+/-0.08	0.48+/-0.06	1.02+/-0.11	Del04	1.86+/-0.07	2.31+/-0.12	2.29+/-0.16	Del04
1999 OJ4	0.99+/-0.08	0.68+/-0.05	1.20+/-0.08	Pei04	1.94+/-0.14a	2.2 +/-0.48	2.46+/-0.16a	Ben11
66652 Borasisi	0.82+/-0.17	0.65+/-0.06	1.30+/-0.06	Ful08	2.01+/-0.07	2.49+/-0.11	2.59+/-0.09	Ful08&
60454 2000 CH105	1.02+/-0.09	0.68+/-0.06		Pei04	2.07+/-0.13a		2.59+/-0.14a	–
2000 CL104	1.22+/-0.17	0.63+/-0.10	1.34+/-0.13	Boe02	2.08+/-0.18a	2.39+/-0.37	2.60+/-0.19a	Ben11
2000 CN105	1.10+/-0.02	0.66+/-0.02	1.3 +/-0.03	Jew07	1.98+/-0.06m		2.22+/-0.33t	Tru11
168703 2000 GP183	0.77+/-0.04	0.39+/-0.04	0.82+/-0.04	Dor02	1.56+/-0.13a		2.08+/-0.15a	–
134860 2000 OJ67	1.05+/-0.06	0.67+/-0.05	1.27+/-0.07	Ful08	1.98+/-0.10	2.26+/-0.14	2.33+/-0.16	Ful08
138537 2000 OK67	0.89+/-0.08	0.65+/-0.05	1.22+/-0.08	Dor02	2.42+/-0.08	2.88+/-0.11	2.92+/-0.12	Del04
2000 QL251			0.85+/-0.09	Ben09	1.59+/-0.15a		2.11+/-0.17a	–
20000 Varuna	0.92+/-0.03	0.61+/-0.02	1.22+/-0.02	Dor07&	1.97+/-0.07	2.53+/-0.10	2.50+/-0.11	Dor07&
88268 2001 KK76	1.03+/-0.06	0.81+/-0.05		Gul06	2.2 +/-0.12a		2.72+/-0.13a	–
2001 QB298				–			2.49+/-0.11a	–
2001 QC298	0.66+/-0.07	0.37+/-0.07	1.00+/-0.06	San09	1.43+/-0.22	1.95+/-0.26	1.89+/-0.26a	San09
2001 QD298	0.97+/-0.13	0.67+/-0.09		Dor05b	2.06+/-0.14a		2.58+/-0.15a	–
2001 QO297		0.69+/-0.11	1.27+/-0.07	San09	2.01+/-0.14a		2.53+/-0.16a	–
2001 QS322				–			2.49+/-0.11a	–

Continued on next page

Table B.1: continued

Name (desination)	B-V	V-R	V-I	Vis Ref	V-J	V-H	V-K	NIR Ref
Teharonhiawako	1.01+/-0.04	0.61+/-0.04	1.25+/-0.05	Osi03	1.99+/-0.13a		2.51+/-0.15a	-
135182 2001 QT322		0.53+/-0.12		Bru09	1.92+/-0.16a		2.44+/-0.17a	-
2001 QX297				-			2.49+/-0.11a	-
2001 RZ143	1.08+/-0.14	0.51+/-0.13	1.00+/-0.12	San09	1.74+/-0.17a		2.26+/-0.18a	-
148780 Altjira	0.91+/-0.13	0.74+/-0.08	1.17+/-0.09	Dor05b	1.91+/-0.15a		2.43+/-0.17a	-
2001 XR254			1.04+/-0.11	Ben09	1.78+/-0.16a		2.3 +/-0.18a	-
126154 2001 YH140				-			2.49+/-0.11a	-
2002 GV31				-			2.49+/-0.11a	-
119951 2002 KX14		0.62+/-0.02		Bru09&	2.28+/-0.07m		2.64+/-0.20t	Tru11&
50000 Quaoar	0.94+/-0.02	0.67+/-0.02	1.28+/-0.02	DeM09&	2.18+/-0.06	2.54+/-0.06	2.57+/-0.06	DeM09&
2002 VT130	1.45+/-0.21	0.56+/-0.10	1.19+/-0.10	San09	1.93+/-0.16a		2.45+/-0.17a	-
2003 GH55	1.12+/-0.05	0.63+/-0.06		Jew07	2.02+/-0.13a		2.54+/-0.13a	-
2003 QA91				-			2.49+/-0.11a	-
2003 QA92				-			2.49+/-0.11a	-
2003 QR91				-			2.49+/-0.11a	-
2003 WU188				-			2.49+/-0.11a	-
120347 Salacia			0.87+/-0.01	Ben09&	1.61+/-0.12a		2.14+/-0.15t	Tru11
2004 VZ75				-			2.49+/-0.11a	-
2005 EF298				-			2.49+/-0.11a	-
303712 2005 PR21				-			2.49+/-0.11a	-
145452 2005 RN43	1.03+/-0.07		1.13+/-0.21	DeM09&	1.59+/-0.05	1.86+/-0.06	2.05+/-0.06	DeM09&
2006 HW122				-			2.49+/-0.11a	-
275809 2001 QY297	0.70+/-0.12	0.43+/-0.09	1.10+/-0.19	Dor07	1.82+/-0.08	2.33+/-0.13	2.37+/-0.39a	Dor07
2007 TY430	1.29+/-0.01	0.74+/-0.01	1.37+/-0.01	She12	1.77+/-0.09		2.05+/-0.28t	She12

a - calculated from average colors of cold classical sample.

t - calculated by J-K from Trujillo et al. (2011).

m - photometry from mixed sources..

& - spectra available.

Reference abbreviations for published photometry tables: Ben09 Benecchi et al. (2009); Ben11 Benecchi et al. (2011); Ben11 Benecchi et al. (2011); Bru09 Brucker et al. (2009); Del01 Delsanti et al. (2001); Del04 Delsanti et al. (2004); DeM09 DeMeo et al. (2009); Dor05 Doressoundiram et al. (2005); Dor07 Doressoundiram et al. (2007); Fra12 Fraser and Brown (2012); Ful08 Fulchignoni et al. (2008); Gru09 Grundy et al. (2009); McB03 McBride et al. (2003); Mul10 Müller et al. (2010);

Table B.2: Colors published in Trujillo et al. (2011)

Name/designation	J-H ₂ O	J-CH ₄	J-K
2000 CN105	0.09+/-0.09	-0.28+/-0.2	0.24+/-0.45
119951 2002 KX14	-0.04+/-0.09	0.13+/-0.1	0.36+/-0.26
50000 Quaoar	0.11+/-0.03	0.27+/-0.04	0.50+/-0.16
120347 Salacia	0.22+/-0.06	0.2 +/-0.07	0.53+/-0.11
2007 TY430 ^s	-0.16+/-0.13	0.07+/-0.15	0.28+/-0.37
s - Sheppard (2012)			

Pei04 Peixinho et al. (2004); San09 Santos-Sanz et al. (2009); She12 Sheppard (2012); Sta08 Stansberry et al. (2008); Tru11 Trujillo et al. (2011); Vil12 Vilenius et al. (2012)

Table B.3: *HST* photometry

Name (desination)	F555W-F675W	F555W-F814W	F555w-F110w	F606w-F814w	F814w-F139m	F139m-F154m	F110W-F160W	Source
66652 Borasisi			1.57+/-0.12a				0.58+/-0.09	Ben11
2001 QC298				-0.43+/-0.06	-1.03+/-0.07	-0.26+/-0.08	0.61+/-0.18	Ben11, Fra12
145452 2005 RN43				-0.13+/-0.01	-1.1 +/-0.01	-0.24+/-0.01		Fra12
Teharonhiawako				-0.07+/-0.05	-1.05+/-0.06	-0.19+/-0.06		Fra12
88268 2001 KK76				0.072+/-0.06	-0.88+/-0.07	-0.15+/-0.07		Fra12
2001 QS322				-0.01+/-0.08	-1.04+/-0.1	-0.15+/-0.12		Fra12
2001 QX297				0.066+/-0.06	-1.01+/-0.08	-0.29+/-0.09		Fra12
2001 RZ143				-0.07+/-0.05	-0.99+/-0.06	-0.27+/-0.07		Fra12
2006 HW122				-0.05+/-0.1	-0.93+/-0.13	-0.48+/-0.18		Fra12
2003 GH55				-0.02+/-0.04	-0.88+/-0.04	-0.25+/-0.05		Fra12
79360 Sila-Nunam			1.57+/-0.25a				0.57+/-0.09	Ben11
19521 Chaos			1.57+/-0.25a				0.55+/-0.03	Ben11
168703 2000 GP183	0.6 +/-0.06	0.92+/-0.06						Ben11
48639 1995 TL8			1.57+/-0.25a				0.64+/-0.03	Ben11
1996 TK66	0.81+/-0.08	1.14+/-0.08						Ben11
1999 CD158			1.57+/-0.25a				0.59+/-0.05	Ben11
1999 OJ4			1.57+/-0.25a				0.34+/-0.1	Ben11
60454 2000 CH105	0.75+/-0.1	1.27+/-0.11						Ben11
2000 CL104	0.66+/-0.09	1.19+/-0.08	1.47+/-0.07				0.64+/-0.11	Ben11
134860 2000 OJ67			1.57+/-0.25a				0.55+/-0.1	Ben11
138537 2000 OK67	0.71+/-0.06	1.07+/-0.05	1.66+/-0.09				0.61+/-0.06	Ben11
2003 QA92				-0.05+/-0.03	-0.99+/-0.04	-0.22+/-0.05		Fra12
2000 QL251				0.6 +/-0.07				Ben09

a - Average F555W-F110W (2000CL104, 2000 OK67).

C. Photometric plots

Spectral plots, albedo as a function of wavelength, for all objects in the sample are presented here. The plots are grouped by availability of photometric data and success of IRAC observation.

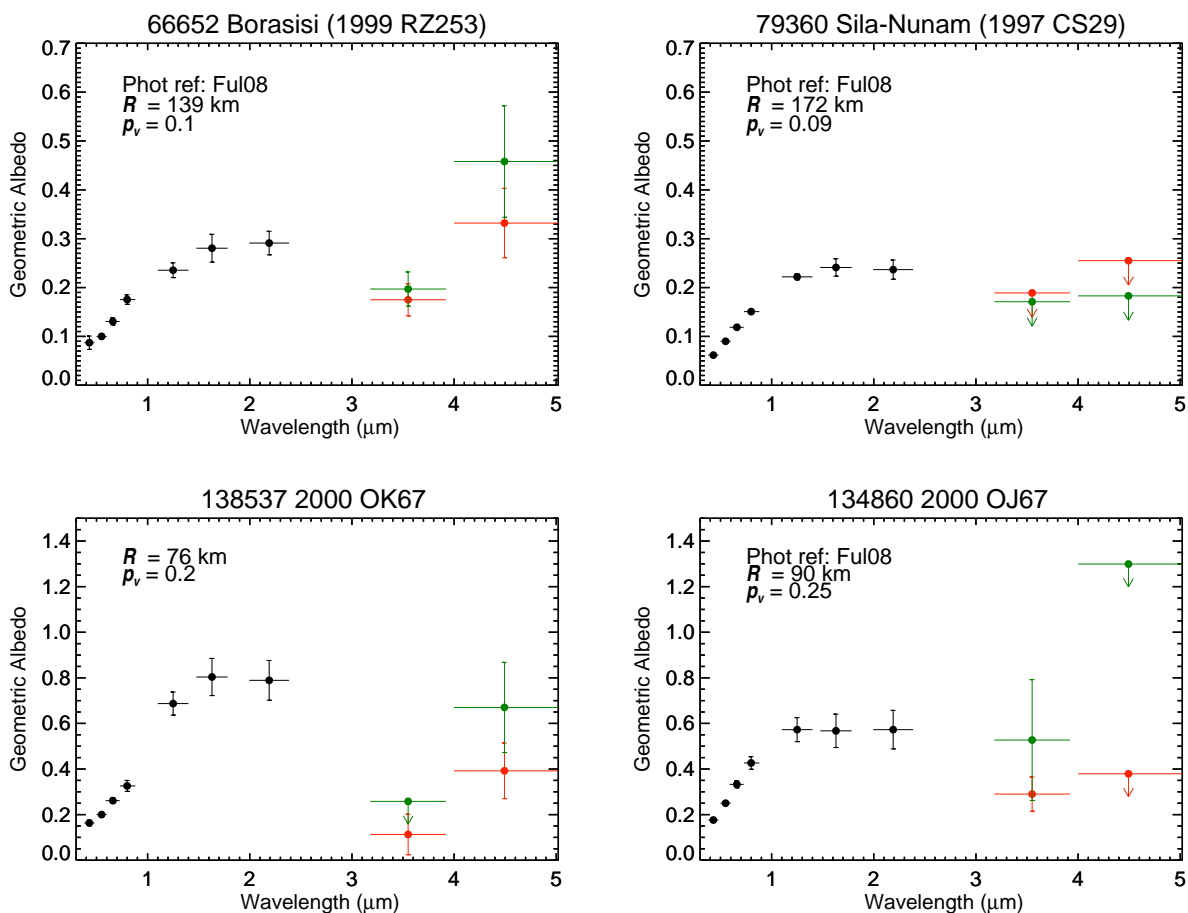


Figure C.1: Cold classical KBOs with published K-band data. Black circles are published photometric data. Green and red circles are IRAC observations. Arrows denote upper limits.

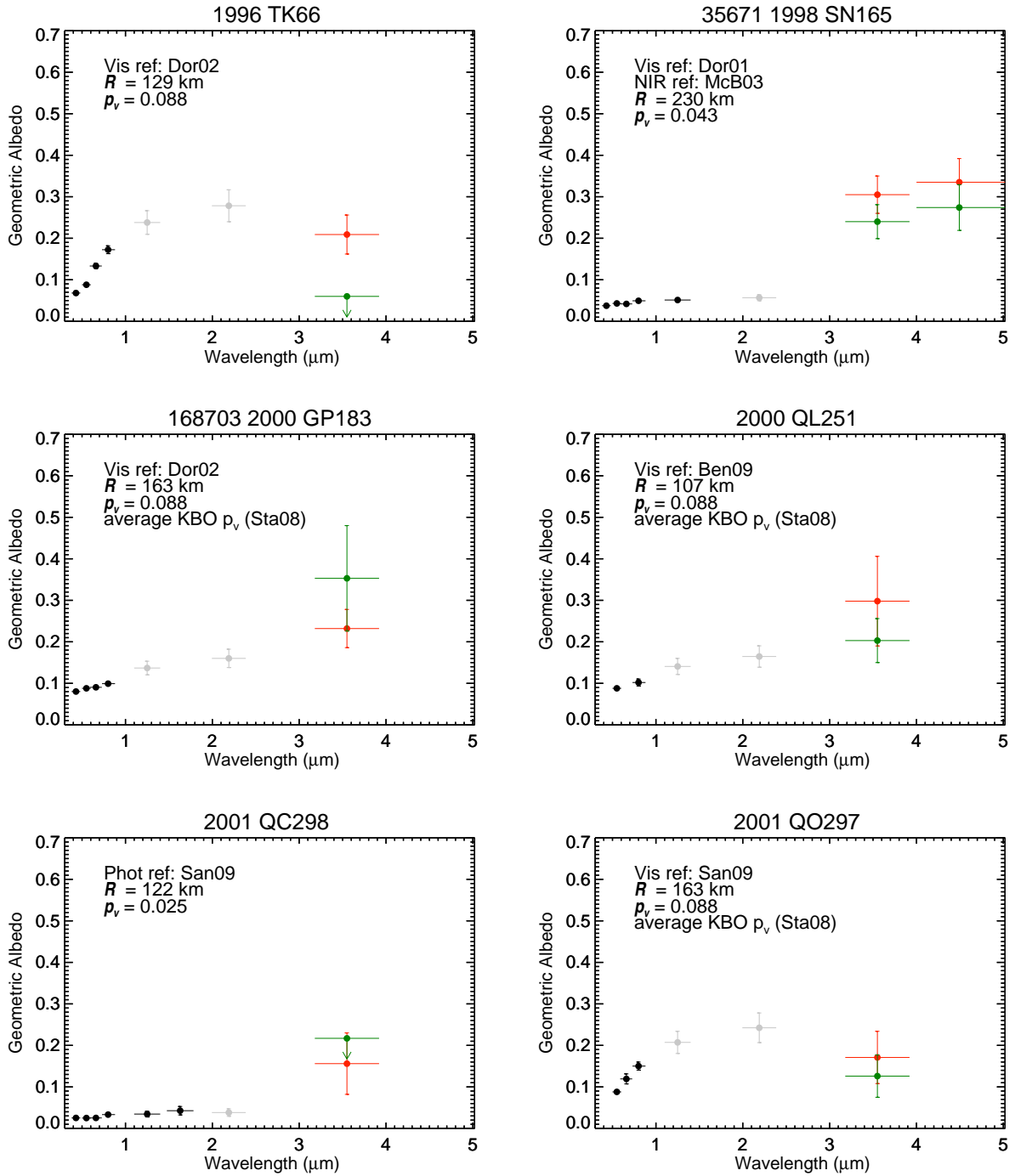


Figure C.2: Cold classical objects with published photometry but no K-band data. Black circles are published photometry, grey circles are averaged photometry. Green and red circles are IRAC observations.

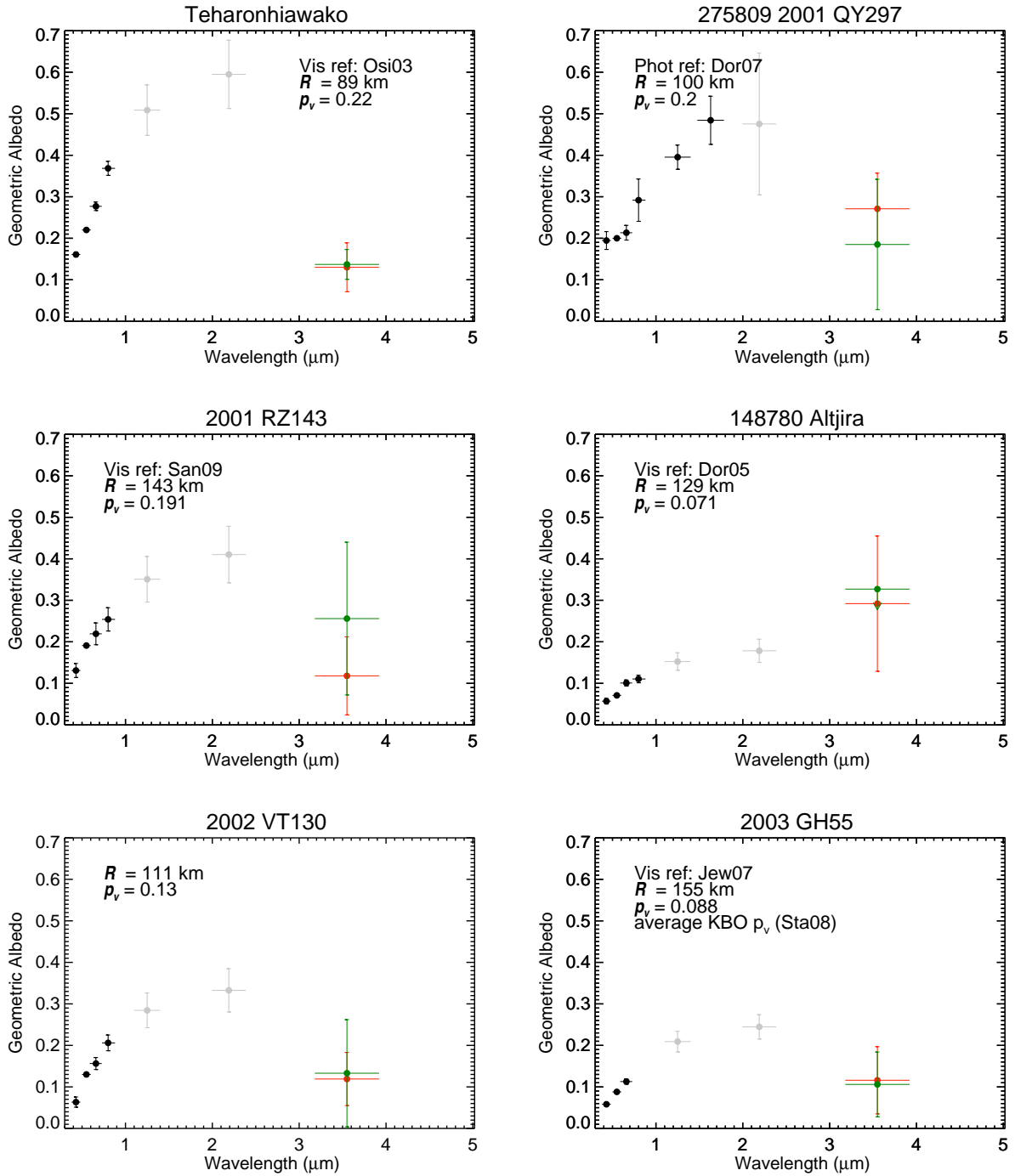


Figure C.3: Cold classical objects with published photometry but no K-band data, continued. Black circles are published photometry, grey circles are averaged photometry. Green and red circles are IRAC observations.

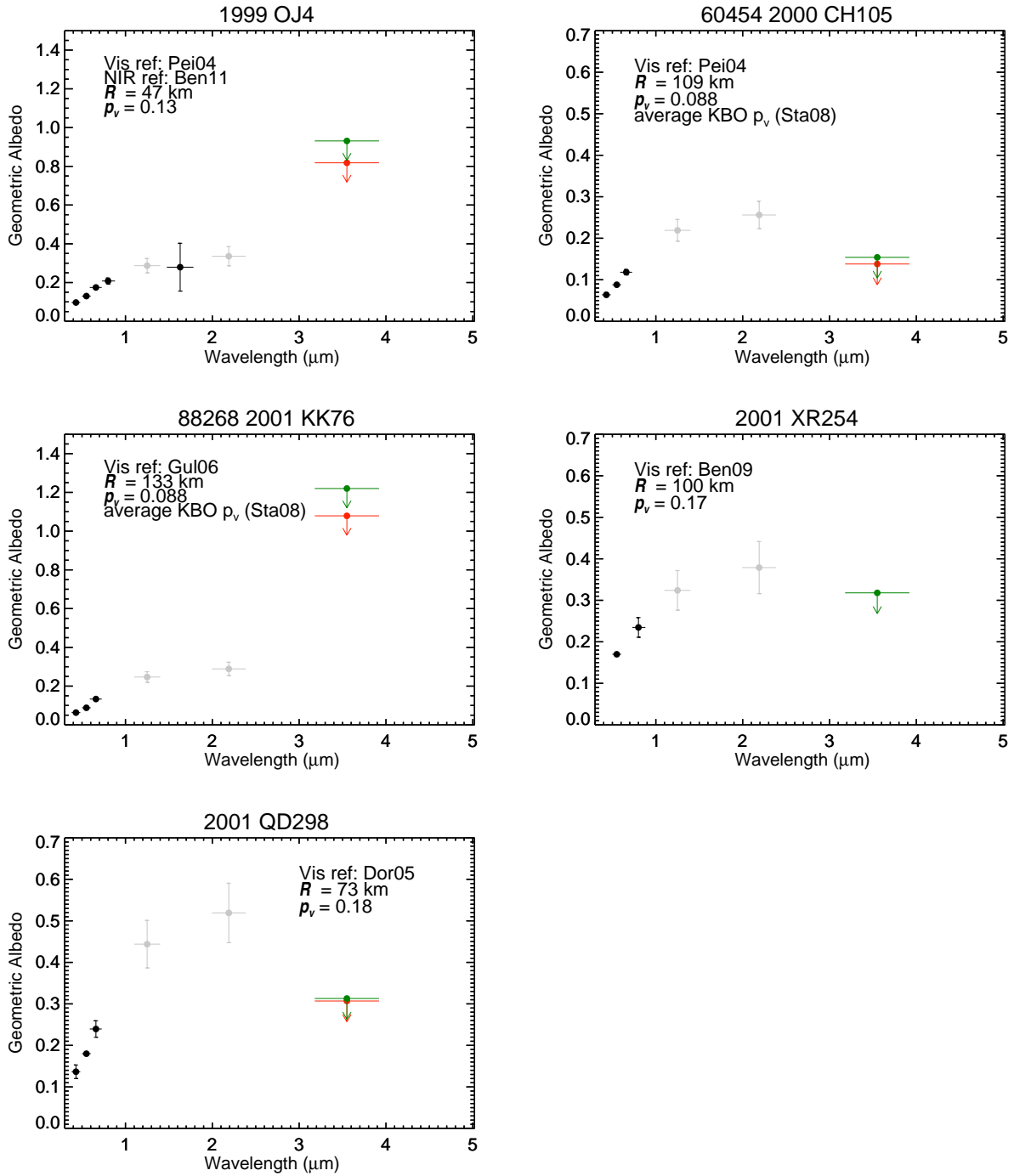


Figure C.4: Cold classical objects with some photometry available, but only upper limit IRAC observations. Black circles are published photometry, grey circles are averaged photometry. Green and red arrows are IRAC upper limits.

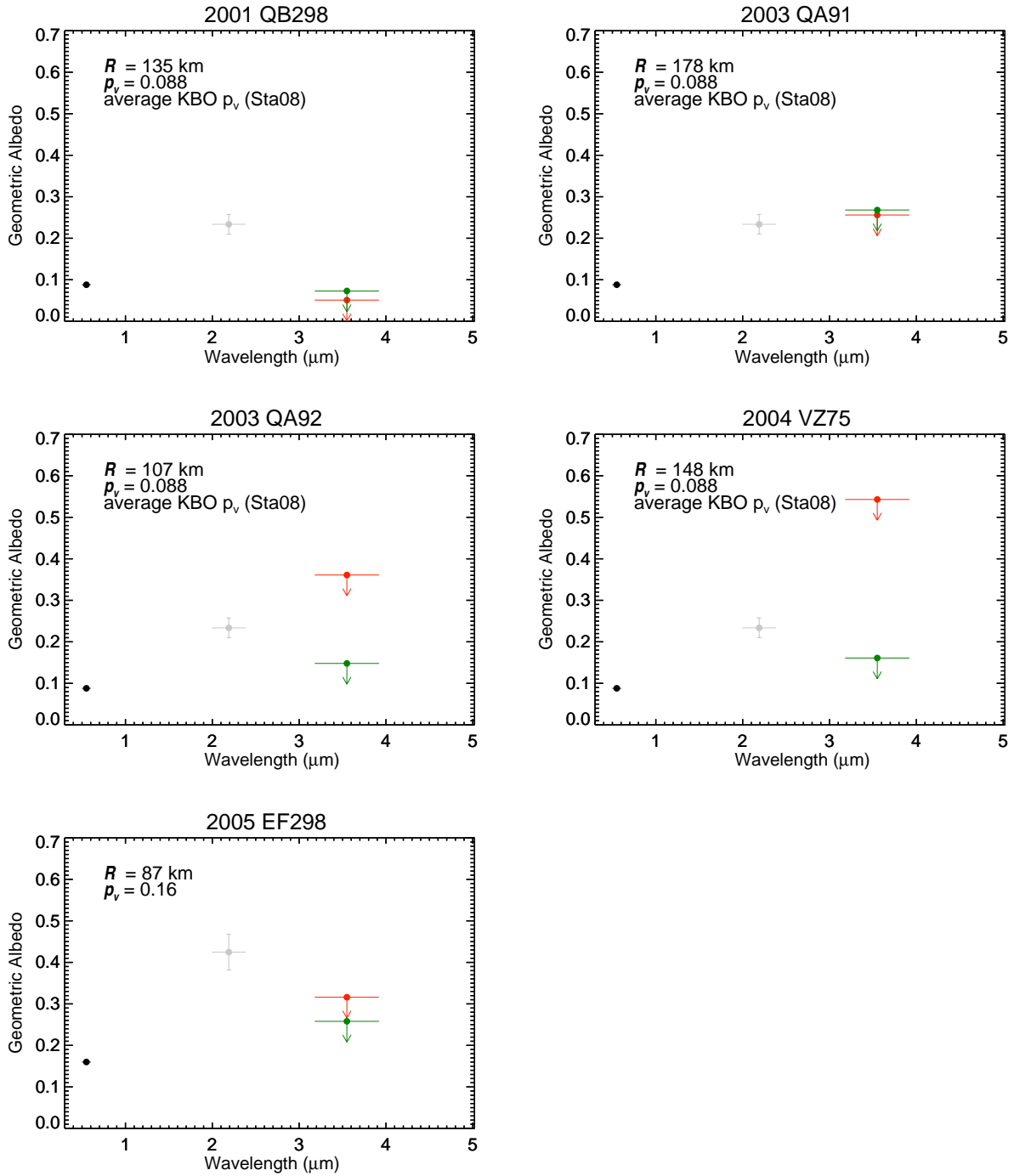


Figure C.5: Objects with no published photometry and only upper limit IRAC observations. Black circles are p_v from literature, grey circles are averaged K-band based on average V-K color of sample. Green and red arrows are upper limit IRAC observations.

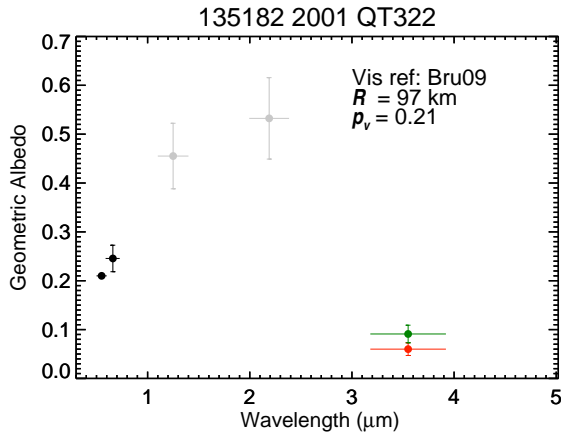


Figure C.6: Cold classical object, 135182 2001 QT322 has some published photometry but no K-band data. Black circles are published photometry, grey circles are averaged photometry. Green and red circles are IRAC observations.

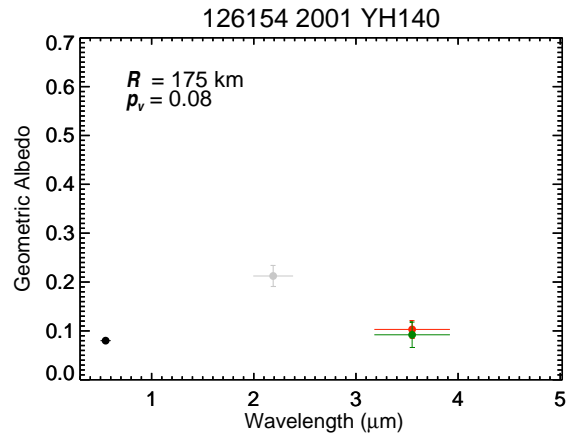
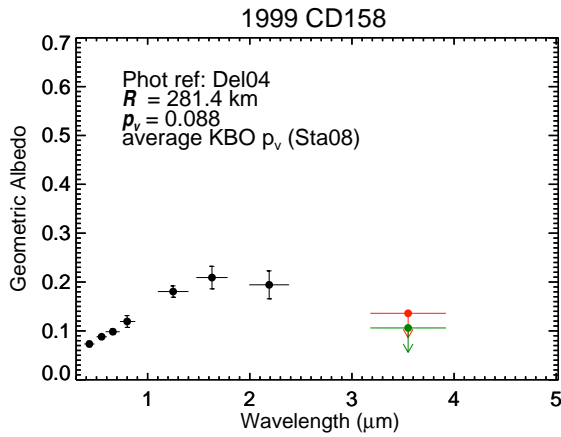


Figure C.7: Photometric plots of objects in MMR with Neptune. 1999 CD158 is in the 7:4 resonance and 126154 2001 YH140 is in the 5:3 resonance. Black circles are published photometry or p_v , grey circles are averaged photometry. Green and red circles are IRAC observations.

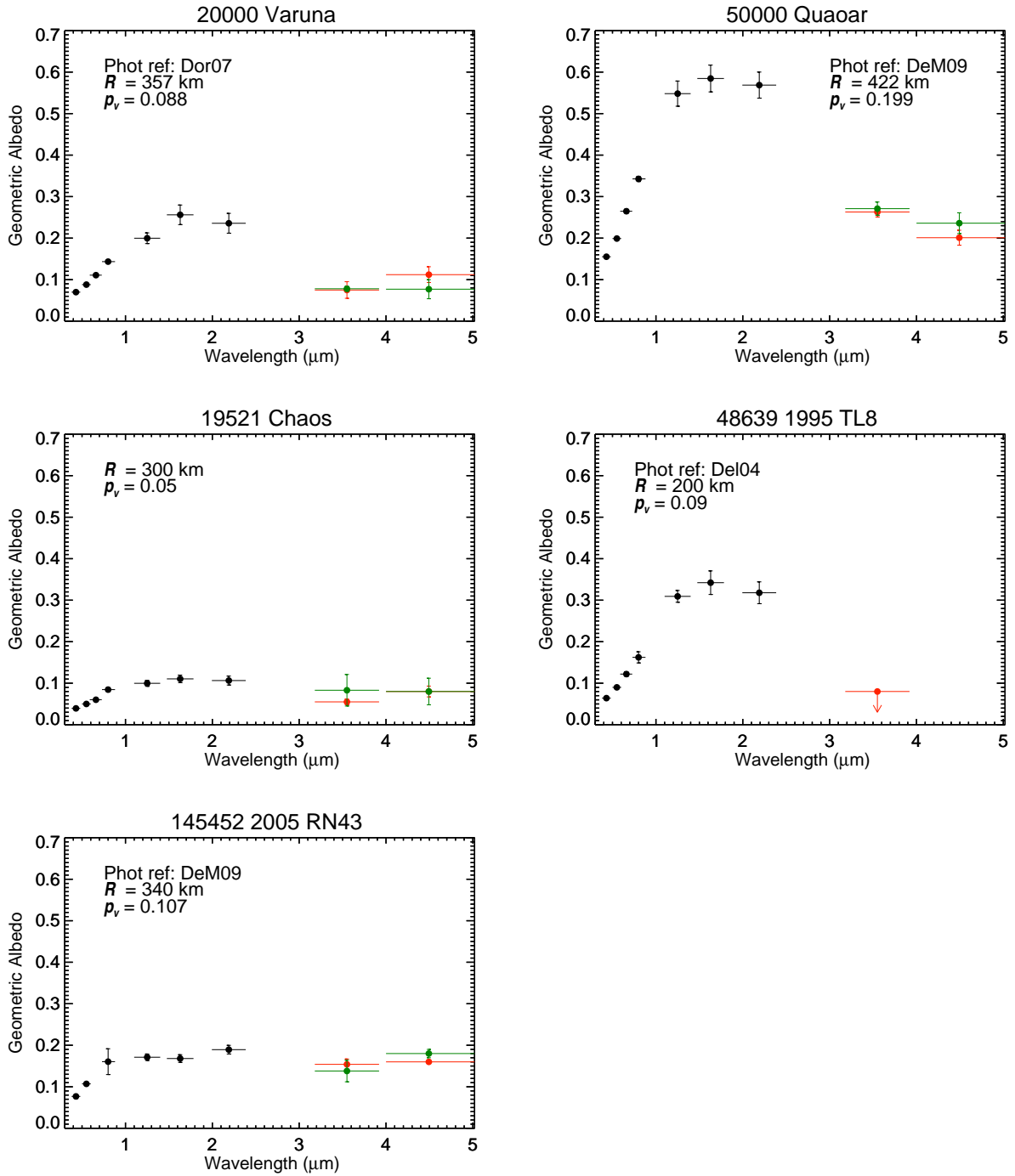


Figure C.8: Additional objects fitting classification scheme set forth in Petit et al. (2011). Black circles are published data. Green and red circles are IRAC observations.

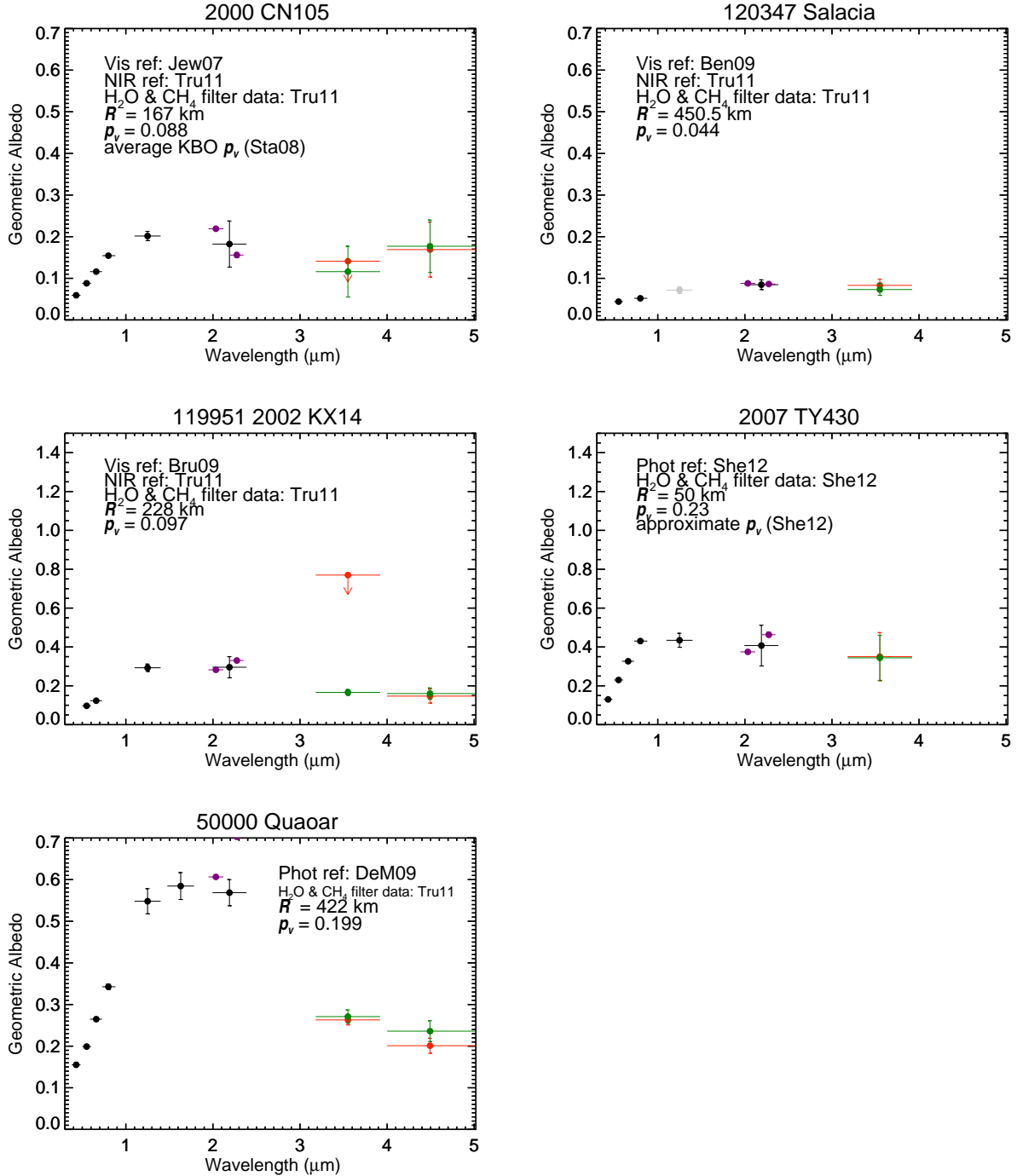


Figure C.9: Objects observed with custom filters described in Trujillo et al. (2011), purple circles. J-band and transformations of the CH₄ and H₂O bands to K-band are plotted, black circles at 1.25 and 2.2 μ m. Data for Quaoar are shown for comparison, however JHK-band photometry published in DeMeo et al. (2009) is plotted.

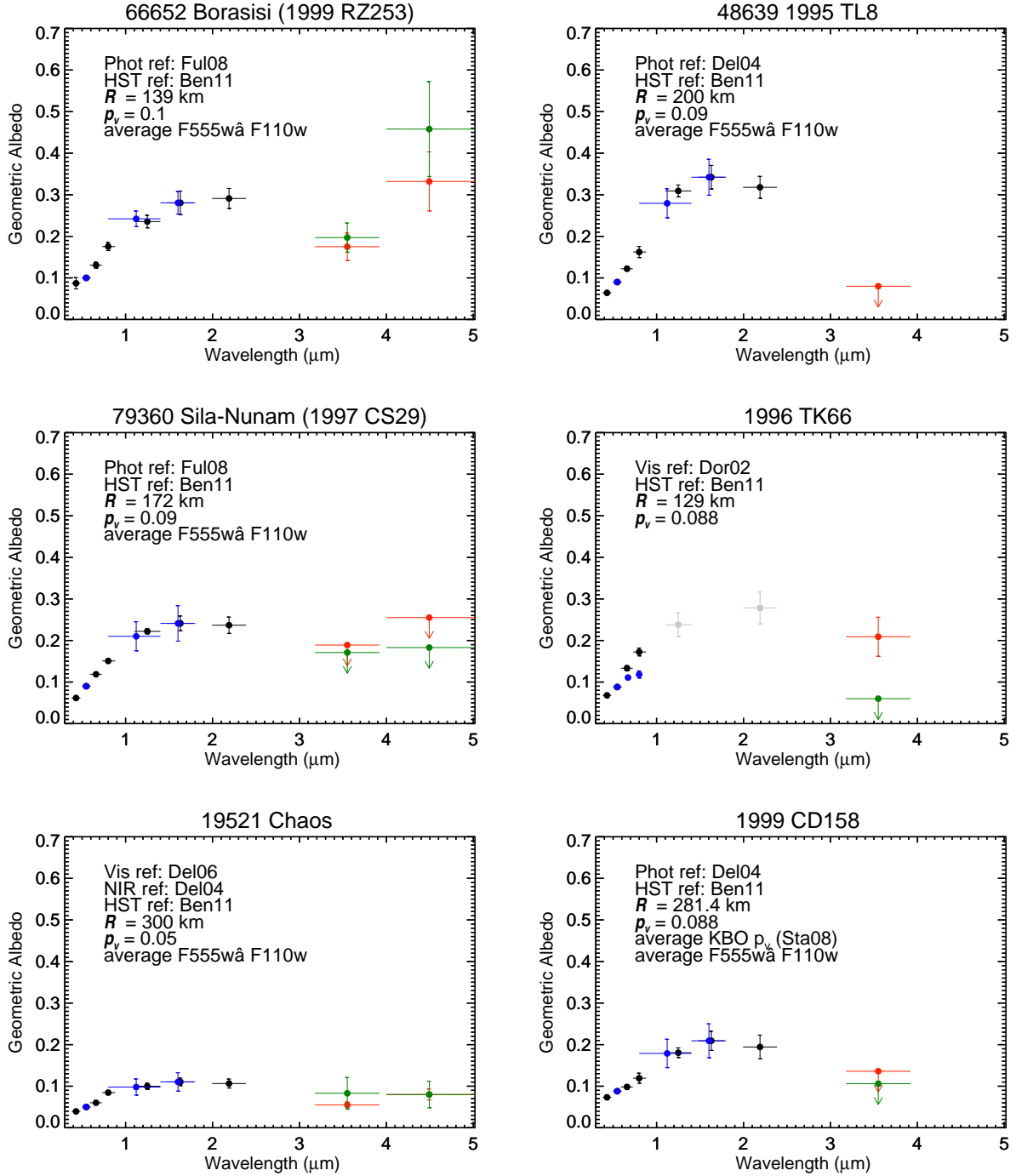


Figure C.10: *HST* data from Benecchi et al. (2011). Blue circles are from *HST* photometry, black circles are VIS-NIR published photometry, grey circles are averaged photometry. Red and green circles are IRAC observations. The *HST* data have been scaled to the vis-NIR, where possible.

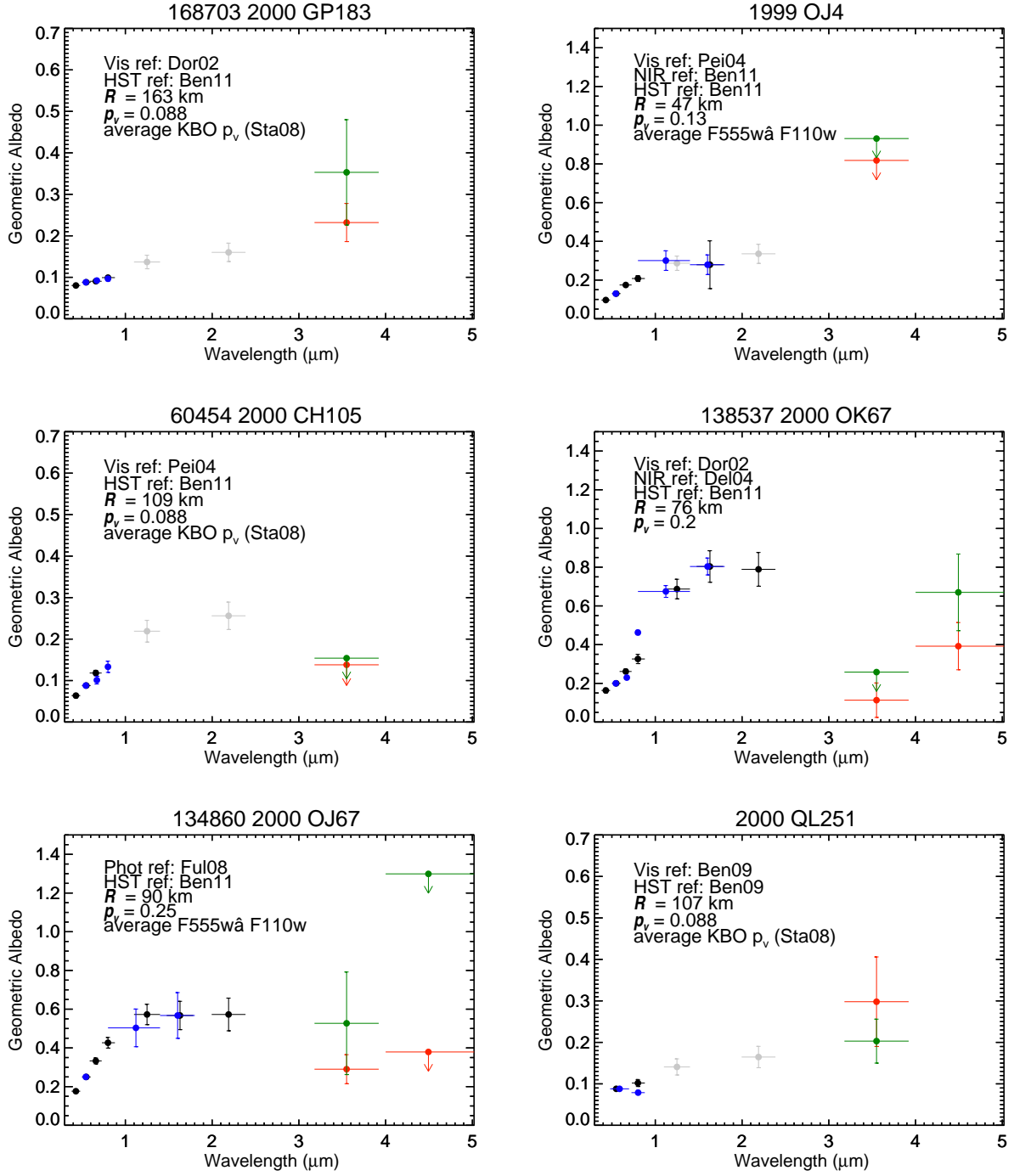


Figure C.11: *HST* data from Benecchi et al. (2009, 2011). Blue circles are *HST* photometry, black circles are vis-NIR published photometry, grey circles are averaged photometry. Red and green circles are IRAC observations. The *HST* data have been scaled to the vis-NIR, where possible.

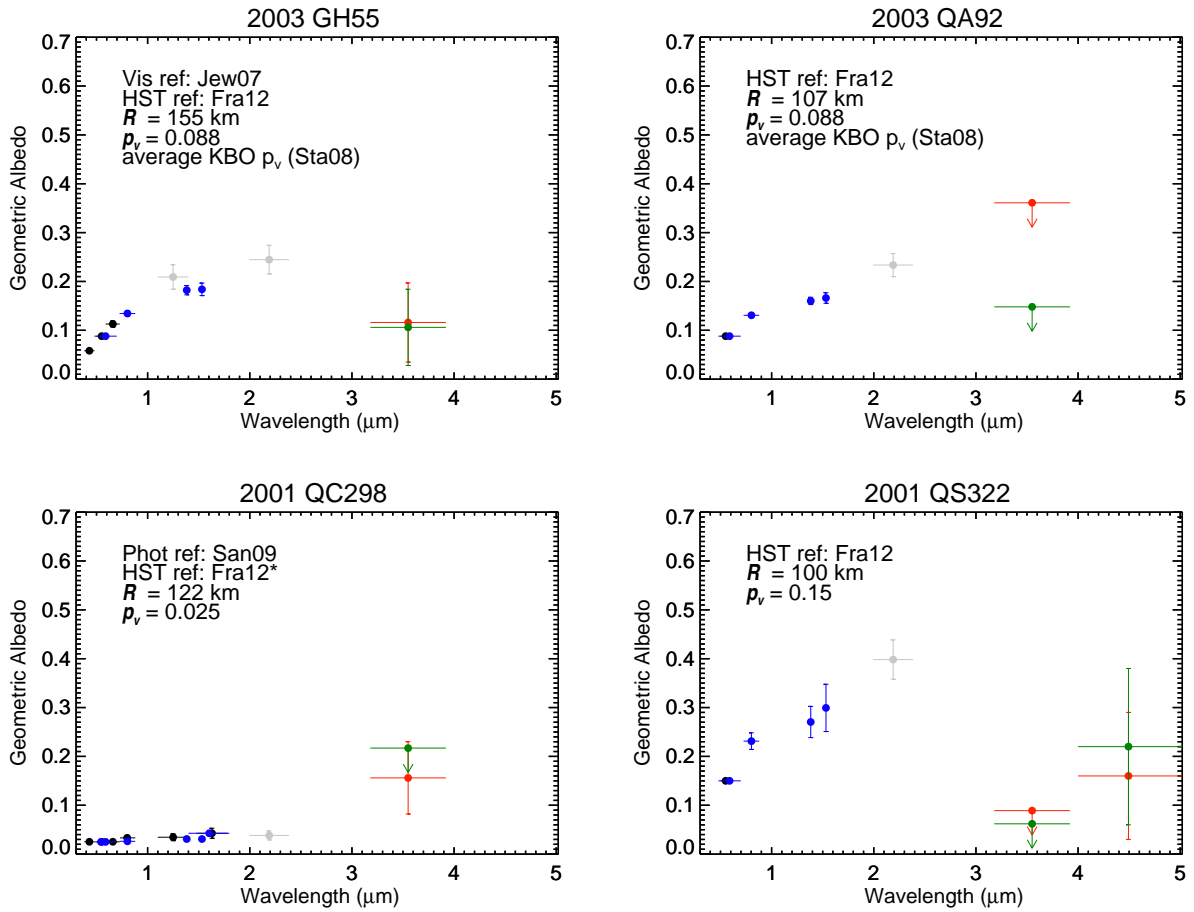


Figure C.12: *HST* data from Fraser and Brown (2012). Blue circles are *HST* photometry, black circles are vis-NIR published photometry, grey circles are averaged photometry. Red and green circles are IRAC observations.

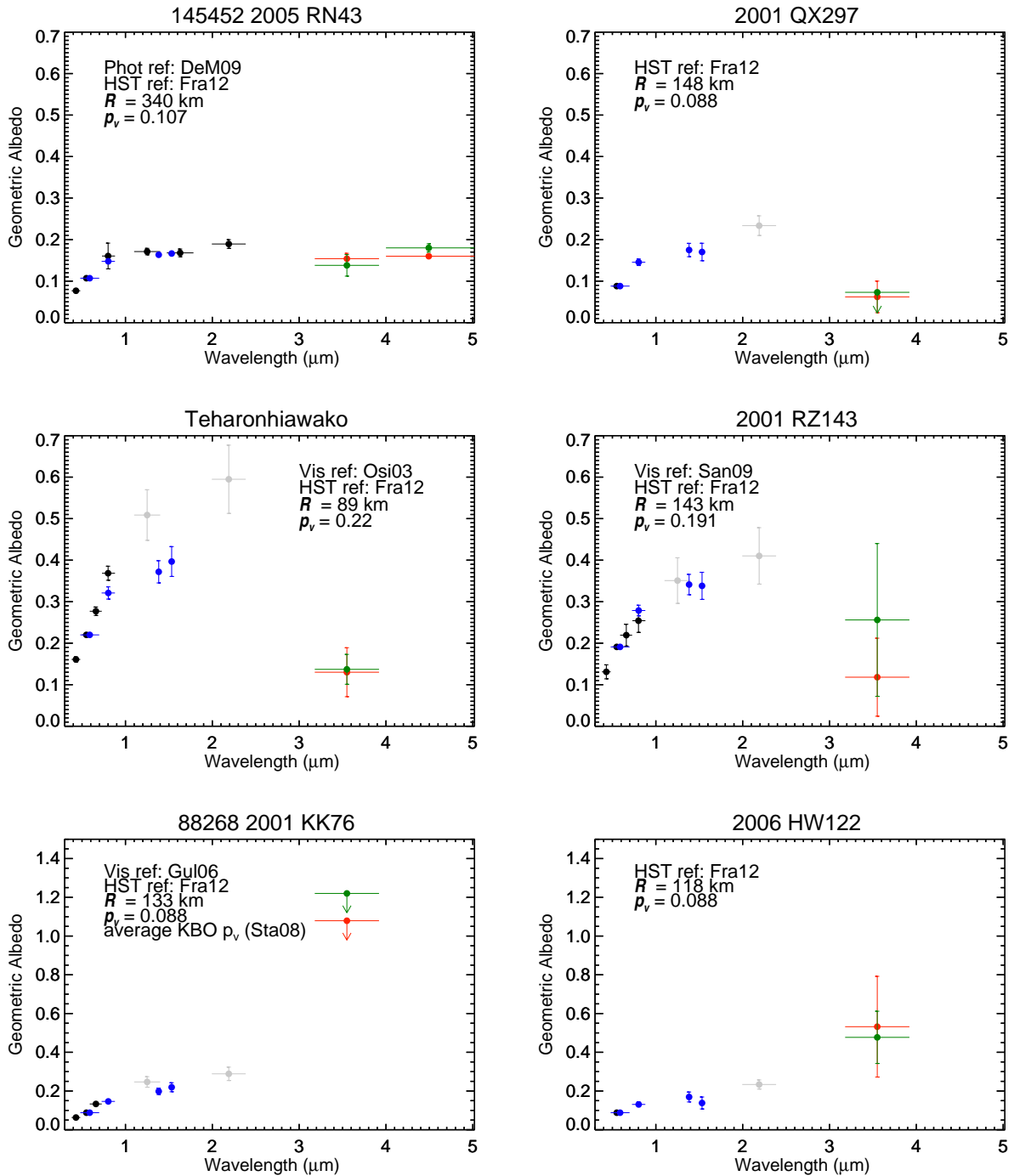


Figure C.13: *HST* data from Fraser and Brown (2012), continued. Blue circles are from *HST* photometry, black circles are VIS-NIR published photometry, grey circles are averaged photometry. Red and green circles are IRAC observations.

D. Database of KBO literature

During the process of finding references for published photometry of KBOs, a large database of references and the values therein was created. The database records many values per object, such as classification and taxonomy, orbital parameters, photometric fluxes and colors, binary and rotation periods, availability of vis-NIR spectra, radii, visible albedo, and beaming parameter, along with the sources of each datum. A list of all available publications for each objects is compiled and then collapsed into one record. The database is able to be searched and sorted at the users discretion. The hope is this database will serve as a tool to enhance literature reviews of KBOs, whether specifically or in groupings, for our team and other future workers. With knowledge of a database programming language and webpage design, this database could provide a useful resource to the entire KBO community.

The cold classical KBOs have been processed into single line entries. Other KBOs, while all publications are collected, have not been reduced fully. More work is needed to bring the database to a more complete level. Some references may have been missed accidentally and typographical errors are surely present. As more papers are published, they could be included in the database. To date, the database contains 6658 entries, 1800 objects, 203 references, and 97 parameters.

Vita

After five years in the U.S. Marine Corps, Daine Wright came to the University of Tennessee to pursue a higher education degree. Looking for a wide base of scientific knowledge, he completed a minor in physics and worked with Drs. Soren Sorensen and Thomas Handler in high energy physics analyzing High Energy Physics data from FOCUS experiment, creating benchmark background of Galactic Cosmic Rays for NASA, programming background simulations for Double-CHOOZ detector, and running efficiency simulations of particle collisions in the PHENIX experiment. Daine took a planetary science class with Dr. Jeffrey Moersch in the department of Earth and Planetary Science and realized Solar System astronomy was his true interest. While completing a Bachelors in Geology, he began to study volatile ices on the surfaces of cold classical Kuiper Belt Objects utilizing the *Spitzer Space Telescope*. Several projects interested Daine during his graduate career, such as neutron imaging of water imbibition in sandstone cores, mapping weathered basalt flows spectroscopically, and statistical modeling of hyperspectral reflectance data. However, Daines primary focus has been the synthesis of data from *Spitzer Space Telescope* and ground based telescopes to analyze infrared spectra of Kuiper Belt Objects and infer their surface ice compositions. Daine won an award in the Physical Sciences at the University of Tennessee's Exhibition of Undergraduate Research and Creative Achievement in 2010. He was the recipient of the Bill Ross Field Camp Scholarship from the Department of Earth and Planetary Science. He was an Oak Ridge National Laboratory and University of Tennessee Science Alliance Summer Fellow. Daine presented his research at the Division of Planetary Sciences of the American Astronomical Society in 2010 and 2012. He co-wrote on a paper on neutron imaging entitled "Diffusivity and Sorptivity of Berea Sandstone Determined Using Neutron Radiography" to appear in Vadose Zone Journal. He is a member of American

Astronomical Society Division of Planetary Sciences, the American Institute of Physics, and the American Geophysical Union. While at the University of Tennessee, Daine was a departmental representative on the Dean's Student Advisory Council, the secretary of the Canoe and Hiking Club, special events coordinator of the Society of Physics Students, a member of the Earth and Planetary Science Student Association, a note taker for the Office of Disability Services, and a mentor at the Adult Student Services Center.